Engineering Structures 293 (2023) 116589

Contents lists available at ScienceDirect

Engineering Structures

journal homepage: www.elsevier.com/locate/engstruct

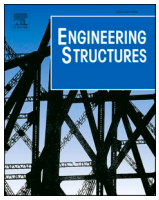

Seismic assessment and strengthening of a historical masonry bridge considering soil-structure interaction

Amirhosein Shabani *, Mahdi Kioumarsi

Department of Built Environment, Oslo Metropolitan University, Pilestredet 35, 0166 Oslo, Norway

ARTICLE INFO

Keywords:
Digital twin
Seismic fragility
Masonry arch bridge
Soil-structure interaction
Operational modal analysis
Seismic strengthening
FRCM systems

ABSTRACT

A holistic methodology for developing the digital twins and conducting seismic vulnerability assessments of masonry arch bridges is proposed and applied to a historical stone masonry bridge. In this light, digital cameras, drones, and 3D laser scanners were utilized for 3D geometric documentation of the bridge. 3D finite element (FE) models were constructed and calibrated based on the operational modal analysis results derived from the accelerometer sensors. The fragility curves for different limit states were derived by performing a multi-stripe analysis (MSA). The effect of soil-structure interaction (SSI) on the calibration results and seismic response of the bridge was evaluated. The results of the visual inspection, model calibration, and seismic analysis revealed that the central pier and the arches are the most susceptible parts of the bridge. Therefore, three strengthening techniques were proposed, and corresponding numerical models were developed. The first model was developed by enhancing the mechanical properties of the vulnerable parts of the bridge, and the two other models were built by covering the central pier's outer surface with polyparaphenylene benzobisoxazole (PBO) and carbon fiber-reinforced concrete mortar (FRCM) layers. Results revealed that the strengthening techniques improved the seismic response of the bridge when subjected to transverse seismic excitations. Negligible differences in the displacement response and crack width of the strengthened models were observed from the nonlinear dynamic analysis.

1. Introduction

Masonry arch bridge conservation is crucial for authorities because of their importance as infrastructure for the road and railway networks and their merit as cultural heritage assets [1]. However, masonry arch bridges are susceptible to earthquake loads because masonry is a brittle construction material, and the bridges are not designed based on current design codes. Moreover, their structural condition has changed due to material decay, fatigue, boundary condition changes, and applied load changes, including higher axle loads and vehicle speeds, since the time that they were built [2]. Masonry bridges comprise around 25% of road bridges and around 45% of railway bridges in Europe [3]. Therefore, a reliable modeling and analysis strategy is required to increase their resiliency.

Efficient numerical modeling and simulation of masonry arch bridges have been an interesting and challenging problem for researchers and structural engineers [4–6]. Masonry arch bridges are heterogeneous structures composed of stone or brick, mortar, and backfill soil that have a distinct architecture due to the presence of arches. Furthermore, finding a solution for considering the effects of masonry and backfill soil interaction and applying appropriate boundary conditions are two pivotal issues that should be taken into account [2,7]. Discrete element modeling is considered the most accurate modeling approach for the nonlinear analysis of masonry arch bridges, with the highest level of computational effort among other methodologies [8,9]. However, by employing acceptable simplifications in the modeling procedure and diminishing the level of computational efforts, the homogenous finite element (FE) method can be an accurate enough solution for seismic analysis of masonry bridges [10–12]. Soil-structure interaction (SSI) effects were usually neglected for nonlinear analysis of various masonry bridges, and fixed base boundary conditions were applied [9,13,14]. Nevertheless, the structure and foundation interaction with the surrounding soil could be influential on the structural response [15]. The inertial interaction effect that causes additional deformations in the soil and changes the base motion is more pronounced for heavy structures such as nuclear power plants and masonry arch bridges [15–19].

Defining a structure's precise material properties is an essential part

* Corresponding author.
E-mail addresses: amirhose@oslomet.no (A. Shabani), mahdi.kioumarsi@oslomet.no (M. Kioumarsi).

https://doi.org/10.1016/j.engstruct.2023.116589
Received 16 January 2023; Received in revised form 16 June 2023; Accepted 9 July 2023
Available online 18 July 2023

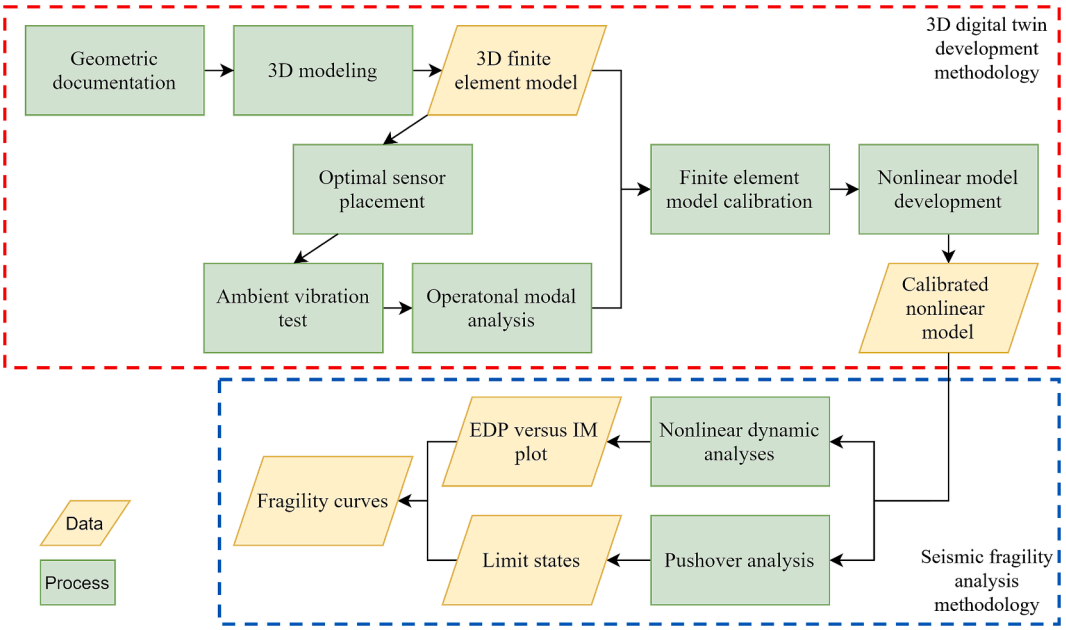

Fig. 1. Methodology of developing 3D digital twins and seismic fragility of historic structures.

of developing its digital twin [20]. However, destructive tests to determine the material properties of masonry arch bridges are usually forbidden because they are considered cultural heritage assets. Furthermore, historical structures suffer from various types of risks that can influence their material properties. For this purpose, calibration of the historical masonry arch bridges model based on the operational modal analysis (OMA) results has recently gained considerable attention [21–24]. The effect of model calibration on the seismic behavior of the masonry structures highlights the importance of this step for developing a robust and accurate numerical model [23,25].

After seismic analyses of the updated numerical models, proposing an efficient and applicable strengthening technique is the final part of an assessment and retrofitting methodology. When retrofitting cultural heritage structures, it is important to follow five key principles: respect for authenticity, minimal structural intervention, compatibility, reversibility (the ability to remove changes), and durability. These guidelines aim to ensure that any changes made to the structure preserve its historical and cultural significance while allowing for its long-term preservation and maintenance [26,27]. However, it is difficult to find a strengthening strategy that satisfies all these rules [26]. A few studies investigated the seismic response of masonry arch bridges strengthened by using fiber-reinforced cementitious matrices (FRCM) [28,29], fiber-reinforced polymer (FRP) composites [30,31], steel anchorage [32], or enhancing the existing masonry mechanical properties [33].

Despite the aforementioned investigations, some gaps can be found, including limitations regarding the SSI effects, numerical modeling aspects, and strengthening strategies. The FE model calibration of a masonry tower, considering SSI effects and comparing the results with the calibrated fixed base model, was investigated by performing a linear time history analysis [34]. Nevertheless, a research study is required to investigate the SSI effects on the seismic behavior of masonry arch bridges, considering the material properties' nonlinearity. Furthermore, because of the high computational efforts involved in the nonlinear analysis of full-scale masonry bridges, the seismic analysis of these structures was typically limited to applying a number of seismic records instead of performing a seismic fragility analysis based on the nonlinear analysis of a group of records with different intensities and properties. The strengthening proposals have also been limited to the retrofitting of spandrel walls or arches of the bridges, and a numerical investigation focusing on the strengthening of the eroded piers of the bridges should be carried out. In this paper, a methodology for deriving the seismic fragility curves of masonry arch bridges for different limit states is proposed and applied to a case study. Accurate geometric documentation of the bridge was done, and two 3D FE models were created for further analysis; in one of them, the SSI is considered, but in another model, the effect was neglected by considering rigid boundary conditions. On the other hand, ambient vibration tests (AVT) were carried out to determine the dynamic characteristics of the case study. FE model calibration was performed for both models, and the material properties were updated. Nonlinear analyses were performed on a model with SSI to obtain the fragility curves. A comparative study was performed to investigate the effect of considering the SSI effects during the whole process. Vulnerable structural parts were detected after seismic damage assessment and three different strengthening techniques were proposed. 3D models of the strengthened bridges were developed, and nonlinear analyses were performed to investigate the efficiency of the strategies.

2. Methodology and overview of the case study

2.1. Methodology

Geometric documentation of a structure is essential for developing digital twins, and various methods have evolved to automate this step in the fastest and most accurate way using different types of digital sensors and instruments. After deriving the geometries, the 3D FE model is constructed, and initial material properties are assigned to different parts based on the empirical equations or limited experimental tests on the construction material.

The material properties of the FE model are calibrated to match the modal properties of the FE model with those recorded experimentally. AVT is used to determine the structure's modal properties. Next, the natural frequencies and their corresponding mode shapes are defined by performing the OMA [35]. Before performing the AVT, it is recommended to conduct an optimal sensor placement (OSP) analysis to determine the best locations for the accelerometers [36]. The numerical model can be calibrated using one of the various numerical approaches presented to minimize the modal properties of the real structure and the numerical model [37,38]. The whole methodology for developing the 3D digital twin is presented in the red-dotted rectangle of Fig. 1.

To evaluate the seismic performance of the structure, the damage

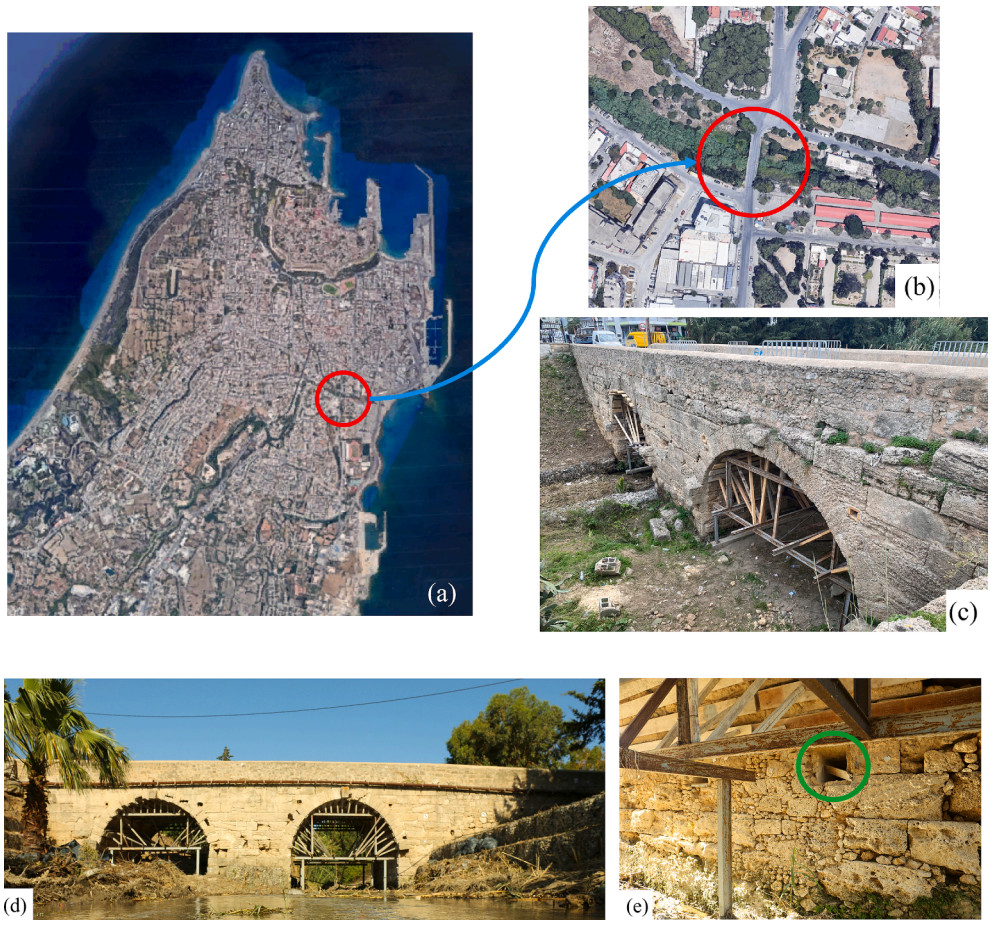

Fig. 2. (a) Rhodes Island in Greece and location of the Roman bridge, (b) top view of the Roman bridge, (c) and (d) Roman bridge from different views, and (e) holes in the central pier with erosion.

limit states are defined by performing a nonlinear pushover analysis. Nonlinear time history analysis is considered the most accurate seismic analysis method, but it requires a high computational effort [39]. A suitable nonlinear material model should be defined for the structure, and nonlinear time history analyses should be carried out by applying seismic records to the structure. The seismic excitations with various intensity measures (IM) are applied to the structure to perform the multi-stripe analysis (MSA) [40]. Seismic fragility curves can also be derived using the efficient methodology by maximizing the likelihood function suggested in [41]. The steps for seismic fragility analysis of the calibrated nonlinear model are illustrated in the blue-dotted rectangle of Fig. 1.

Various strengthening techniques are proposed after defining the most susceptible structural components through the seismic analysis of the calibrated model. Then, corresponding strengthened FE models are developed, and seismic analysis can be performed by applying a set of seismic records that impose a specific damage state on the structure. Finally, a comparative study of the structural demands of the strengthened models reveals the optimal strengthening proposal.

2.2. Overview of the case study

The Roman bridge is on the east coast of Rhodes Island, Greece (see Fig. 2 (a)) and was built across the stream of Rhodini before its outfall to the Mediterranean Sea, as illustrated in Fig. 2 (b). The bridge is 8.4 m wide with two spans of 6.4 m. The thickness of the masonry arch and spandrels is 0.6 m. The bridge was built during the Graeco-Roman era, around the first century BC. Based on the riverbed, the stream only passes through the southern arch, and erosion of the central pier was reported in different old books and diaries [42]. Fig. 2 (c) and (d) show different perspectives of the Roman bridge.

There are two holes on the south side and three on the north side of the bridge's central pier. Fig. 2 (e) highlights one of the holes in a green circle. These holes, with a length and width of 0.4 m and a depth of 0.8 m, may be used as support for the wooden logs. However, these openings can reduce the weight of the structure and diminish the possibility of water flow damage to the structure. However, based on the iron hinges attached to the sides of the holes and the Christian crosses engraved on blocks above one of the holes, it can be concluded that they were later used as storage closets [42].

The Roman bridge is one of the few remaining historical bridges in Greece. The bridge is used by both cars and heavy trucks and is considered one of the main roads in the eastern part of the island. Therefore, the conservation of the bridge is critical not just because of its historical significance but also because of its infrastructural importance as part of the island.

Cracks and spalling of the stone units beneath the arches and vegetation of the central pier and erosion of this part (see Fig. 2 (e)) are the existing damages that were investigated during the visual inspection of the bridge. Temporary scaffolds were built to avoid future damage beneath the arches and spalling stones. A robust and permanent strengthening strategy should be proposed for the preservation of this monumental infrastructure. Rhodes Island is situated in a highly seismic zone with a peak ground acceleration (PGA) of 0.35–0.55 g at a 10% probability of exceedance in 50 years [43], and documentation shows that some of the earthquakes were associated with tsunamis [44]. For this purpose, the presented methodology was applied to this case study to improve its resiliency to earthquake risks.

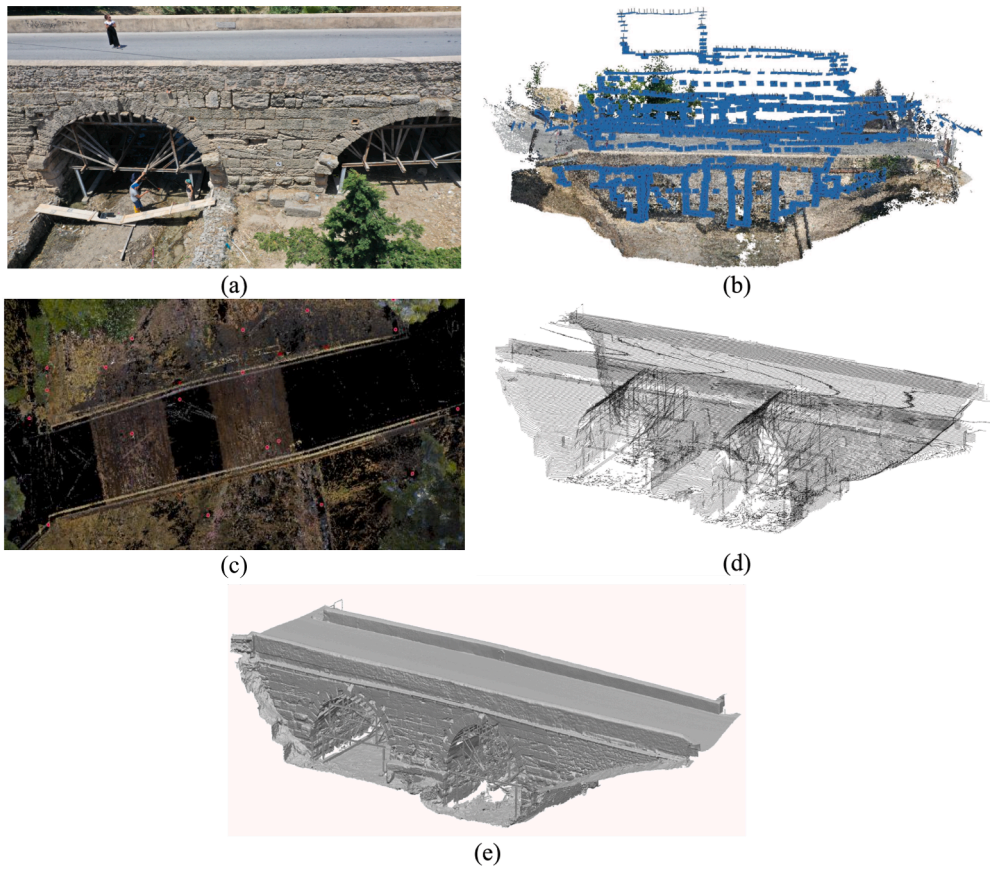

Fig. 3. (a) Geometric documentation campaign, (b) the position of the oriented cameras, (c) dense point cloud, (d) cross-section model, and (c) 3D light model of the Roman bridge.

3. 3D digital twin development of the bridge

3.1. 3D modeling of the bridge

A holistic methodology for deriving the 3D geometric documentation of structures was presented in [45,46]. Aerial images using drones and ground images using cameras are provided for the Roman Bridge, as depicted in Fig. 3 (a). A total of 271 ground digital images were taken, and 2576 aerial images using drones were taken with lower resolution than the ground images because of difficulties in accessing some parts of the structure. Next, the digital images were processed in image-based modeling software through filtering and noise reduction to develop the dense point cloud of the structure. The acquired images were reoriented with high accuracy via the automated structure of the motion process, as depicted in Fig. 3 (b). On the other side, 3D laser scanners are utilized to fill the gaps in the point clouds from the digital images and provide the final dense point cloud. Twenty-four scans were carried out using 3D laser scanners. A local coordinate system was made using two total stations to define target points for the point clouds from laser scanners and ground control points for the orientation of images. Georeferencing avoids possible errors when combining and processing the datasets from different instruments. The final 3D model can be developed by processing the triangulated irregular network representation model in such a way that each point is converted to a polygon object [46]. The 3D dense point clouds, a 3D light model, and the cross sections obtained following this process are illustrated in Fig. 3 (c), (d), and (e), respectively.

For creating the 3D FE model of the bridge, the dimensions were derived from the obtained 3D model from the previous step using DIANA FEA software [47]. Five main parts were considered for modeling the bridge, including arches, spandrel walls, backfill, piers, and parapets, as illustrated in Fig. 4 (a). The foundation and surrounding soils were modeled for modeling the SSI effects, as illustrated in Fig. 4 (b). The holes on two sides of the central pier were also modeled.

Two models were constructed. The first model (fixed-base model) has rigid boundary conditions without modeling foundations and soil media, neglecting the soil-foundation-bridge interaction effects, as illustrated in Fig. 4 (a). The second model (SSI model) was developed using the direct method to consider the SSI effects by modeling the soil and foundation parts, as depicted in Fig. 4 (b) [15]. The soil box was modeled with an equal length and width of 180 m. The depth of the soil was considered 30 m above the bedrock based on [17,48]. Pinned supports were applied to the four sides around the soil and one side at the bottom of the soil box [49–51]. Foundations are also modeled in three positions, embedded in the soil at a depth of 1.5 m beneath the piers.

Contact interface elements with a high initial stiffness value in normal compression and tangential friction with a tension cutoff were modeled to simulate the interaction between backfill and masonry media [1,13]. Therefore, the interface can transform the shear and compression normal stresses, but separation appears in tension between the foundation and the soil media. Although the interface element increases the computational effort by increasing the number of elements, it can simulate the actual interaction and avoid early convergence problems due to the high differences between the stiffness of the two media [52]. The contact interface element between the masonry and backfill soil domains follows the Coulomb friction model in shear with zero cohesion and a friction coefficient of 0.4 rad [53]. The effect of soil-foundation interaction was simulated using a nonlinear interface element [54]. The interface element has high normal and shear stiffness with a tension cutoff.

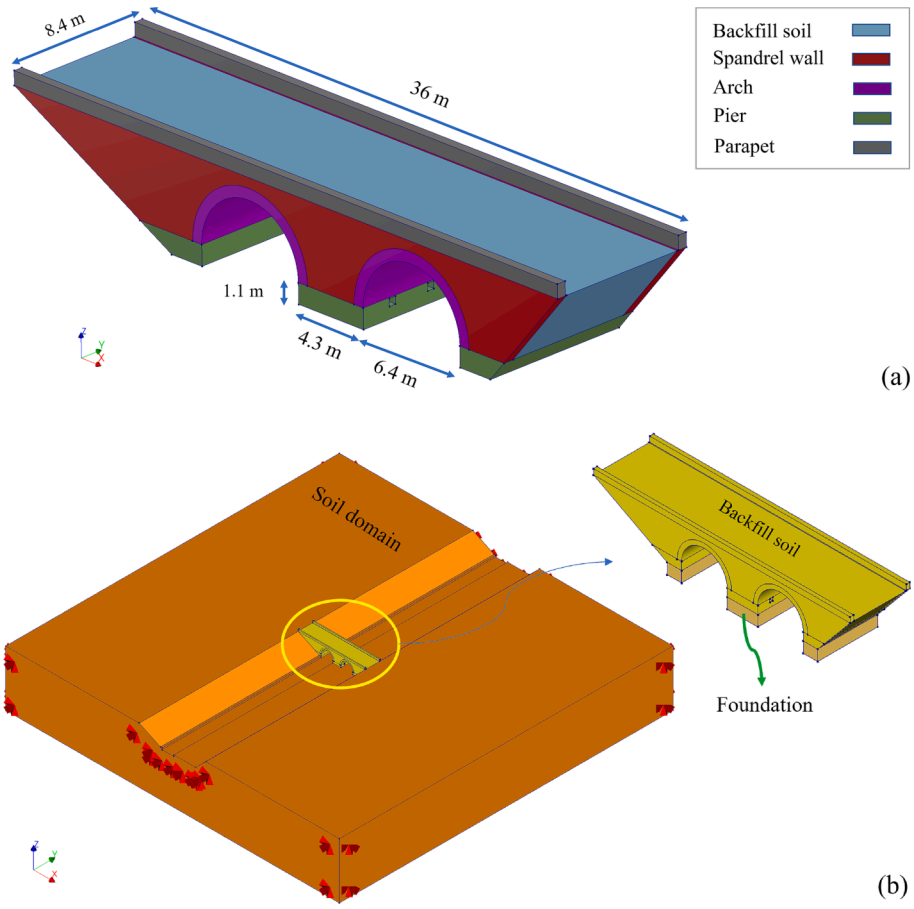

Fig. 4. (a) Fixed-base 3D model with components of the bridge in different colors, and (b) SSI model of Roman bridge.

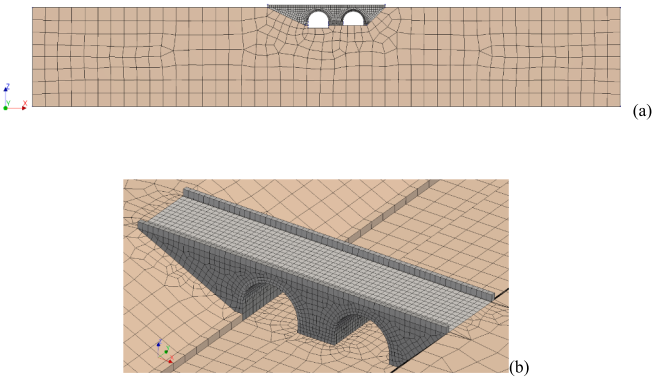

Fig. 5. (a) 3D mesh of the SSI model (b) mesh details of the bridge.

3.2. Initial material properties

The bridge is made of Sfouggaria stone, which is an ancient local stone that was used for the construction of monuments and has a compressive strength (f_b) of 9 MPa [55]. The compressive strength of the homogenized masonry was considered to be 2.503 MPa, calculated based on Equation (1) [56,57], considering soft mortar with compressive strength (f_m) of 1 MPa.

$$f_c = 0.6 f_b^{0.65} f_m^{0.35} \tag{1}$$

The elastic modulus of the masonry was assumed 1001.2 MPa, calculated as 400 times of the f_c [56]. Furthermore, the initial elastic modulus of the backfill soil was assumed to be 0.3 MPa [58]. Hard soil with an elastic modulus of 6 MPa was considered for the soil domain [34]. Note that the density and Poisson ratio of all materials, including the masonry and backfill soil, were considered to be 2200 $\frac{kg}{m^3}$, and 0.3, respectively. Nevertheless, the density of the soil was assumed to be 2000 $\frac{kg}{m^3}$ as suggested in [34].

3.3. Mesh size

Adaptive meshing with a size of 0.6 m was considered for the parapets and backfill soil. After conducting a mesh sensitivity analysis, a mesh size of 0.5 m was used to mesh the spandrel walls and foundations, while a mesh size of 0.4 m was used for the central pier and arches, as shown in Fig. 5. The maximum mesh size of the soil medium was defined based on the following equation [59]:

$$l_{max} \leq \frac{\lambda_{min}}{10} \leq \frac{V_{s,min}}{10 f_{max}} \tag{2}$$

where λ is the wavelength of the passing wave, V_s is the minimum shear wave velocity, and f_{max} is the maximum frequency of interest, typically around 10–15 Hz, as suggested in [59]. A shear wave velocity of 600 $\frac{m}{s}$ for the soil was reported by the responsible partner of the project, and the soil was categorized as hard soil. In order to minimize the maximum size of the mesh elements, 15 Hz was considered for the f_{max}. The maximum mesh size of the soil was set to 4 m, and a finer mesh was considered around the bridge by limiting the mesh size of the edges of the soil part to 2 m, as illustrated in Fig. 5.

The bridge model comprises 13,277 3D mesh elements and 1962 contact interface elements between the backfill and the masonry media. The soil box and the foundations are composed of 49,870 3D mesh

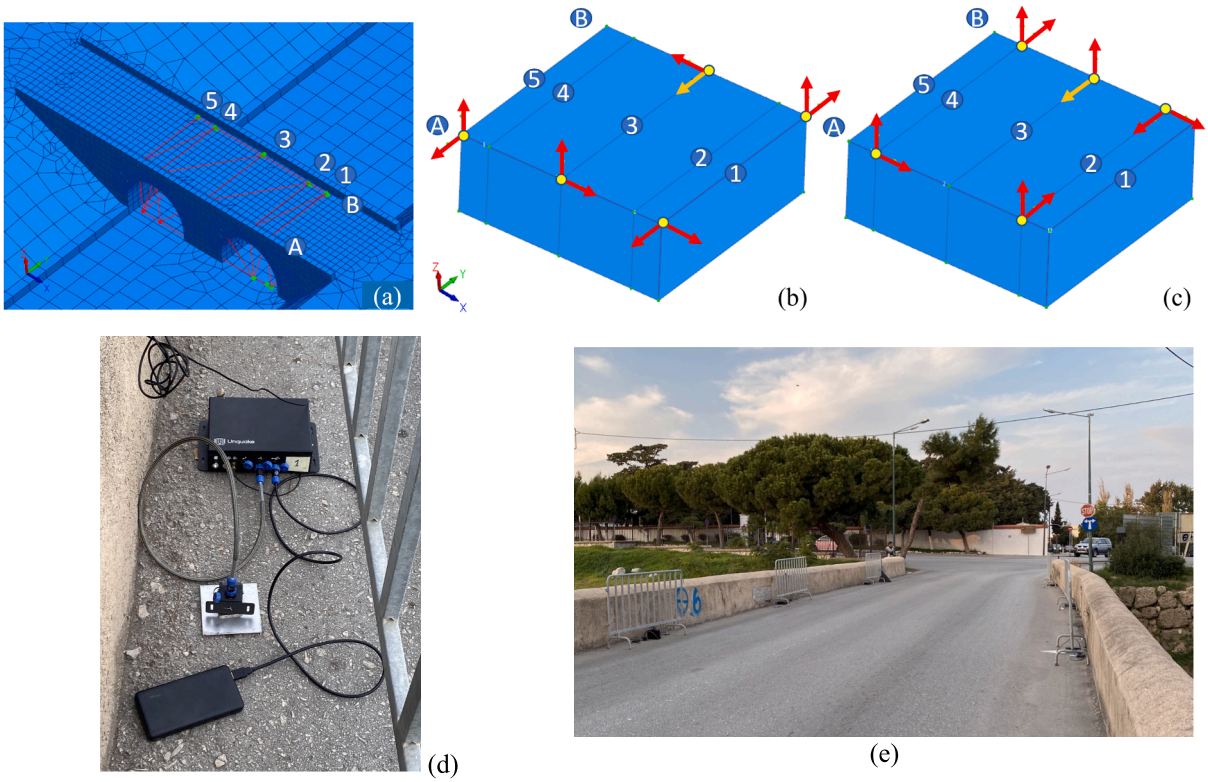

Fig. 6. (a) Optimal sensor locations and sensors' configuration of the (b) first and (c) second test setups. (d) From top to bottom: datalogger, accelerometer sensor, and power bank, and (e) AVT campaign of the Roman Bridge.

elements with 916 contact interface elements to simulate the soil-foundation-structure interaction.

3.4. Ambient vibration testing

After developing the 3D FE model of the bridge with the corresponding material properties for each part, ambient vibration testing was done for modal identification and numerical model calibration.

The accelerometer locations were chosen based on the OSP analyses on the preliminary FE model with the same elastic material properties. The modal assurance criterion (MAC) matrix was considered the acceptance criteria, and five OSP methods were applied to investigate the best sensor locations. The effective independence methods and sensor elimination using MAC are two OSP methods based on the sensor

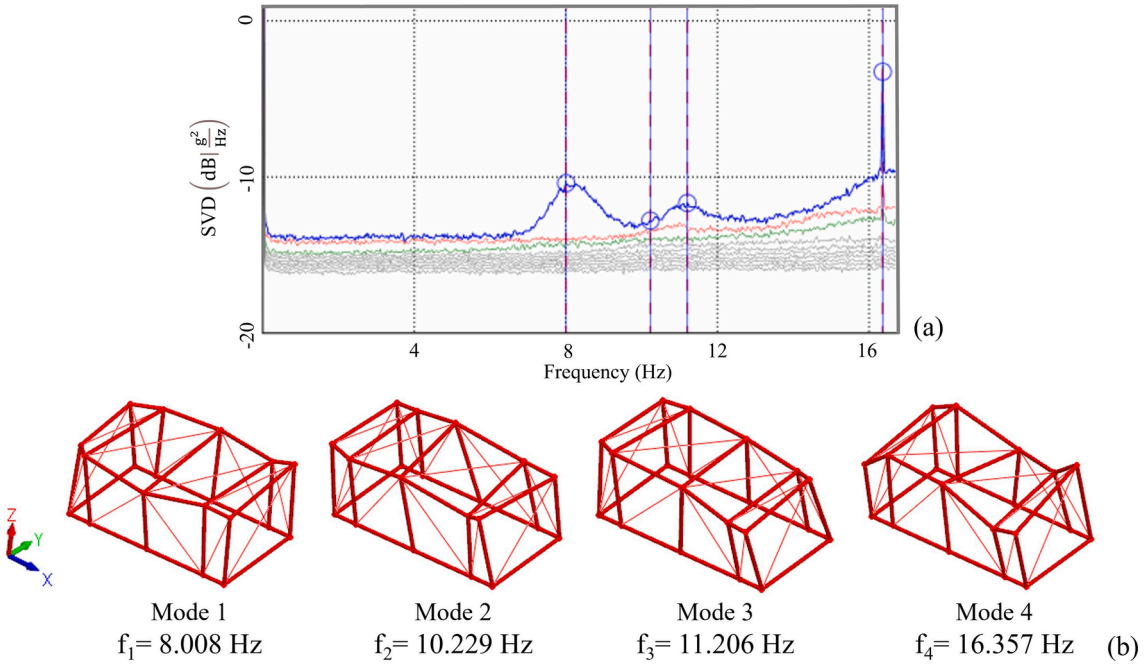

Fig. 7. (a) SVD graph of the FDD method, (b) mode shapes and corresponding frequency values of the first four natural modes of the bridge.

elimination strategies [60]. The MAC matrices of these methods are predominantly diagonal; therefore, these methods reveal the best configuration of the sensors. Therefore, based on the OSP results, the top of the central pier and the locations between the top of the arches and the two endings of the bridge with an approximate distance of 2 m were chosen for installing the sensors. More detail about the procedure can be found in [60].

Fig. 6 (a) shows the optimized locations of the sensors in five rows and on two sides (A and B). Fig. 6 (b) and (c) illustrate the measured direction of the sensors in the first and second test setups. The locations of the outer parts (rows 1 and 5) in the first setup and the inner rows (rows 2 and 3) in the second setup were chosen to install the sensor. However, row 3 was determined to be one of the most important locations prescribed almost by all the OSP analysis results [60]. Row 3, side B in the Y direction, highlighted in Fig. 6 (b) and (c), was selected as the reference measurement direction to combine all the sensors' data from the two test setups.

After determining the best sensor locations, five 3-axis MEMS digital Unquake accelerometers (see Fig. 6 (d) with a sampling rate of 250 Hz were installed on the two sides of the bridge in two test setups. Note that the accelerometers were connected to power banks, as illustrated in Fig. 6 (d), instead of urban electricity to reduce the measurement noise. Because the Z direction of the accelerometer was not sensitive enough to record the ambient vibrations, this direction was neglected from the measurements, and the sensors' data were collected from the two other axes. The data from the sensor in each test setup was synchronized based on the global positioning system (GPS) antenna [34]. Fig. 6 (e) shows the accelerometer sensors installed on two sides of the road.

3.5. Operational modal analysis

Firstly, the fast Fourier transform analysis was performed for each sensor measurement in each direction, and the natural frequency values were detected. To define the mode shapes, all synchronized sensor data from the setups were imported to the ARTeMIS modal software package to perform OMA on a sensor network [61]. Frequency Domain Decomposition (FDD), Enhanced Frequency Domain Decomposition, and Curve-Fitted Enhanced Frequency Domain Decomposition methods are three frequency-domain OMA methods that were employed for the dynamic identification of the bridge [62]. Results reveal a negligible difference between the natural frequency values derived from the three methods mentioned. Fig. 7 (a) depicts the singular value decomposition (SVD) graph of the FDD method and the first four peaks that show the first four natural modes of the bridge. The frequency values and the corresponding mode shapes are illustrated in Fig. 7 (b). The first, third, and fourth modes are predominantly in the Y direction, and the second mode is in the X direction of the bridge.

3.6. Calibration of the model

The objective of the FE model update is to minimize the differences between the natural frequencies of the numerical model and the real structure and to increase the MAC values of the correlated modes by changing the material properties. For this purpose, a sensitivity-based parameter estimation method was utilized using the FEMTools software package [63]. The functional relationship between the parameters and structural modal properties can be expressed in terms of the linear term of a Taylor series expansion as follows:

$$\{\Delta R\} = [S]\{\Delta P\} \tag{3}$$

where ΔR is the difference between a vector containing the reference and predicted system responses, ΔP is the difference between a vector containing the given state and predicted system parameters, and S is the sensitivity matrix. In this paper, a model updating was carried out by minimizing a weighted error (E) according to Equation (4) using the Bayesian parameter estimation expression.

$$E = \{\Delta R\}^t[C_R]\{\Delta R\} + \{\Delta P\}^t[C_P]\{\Delta P\} \tag{4}$$

where C_R and C_P represent weighting matrices expressing confidence in the model responses and parameters, respectively [63]. For the model updating of the bridge, no range was considered for the change of the elastic modulus value [1,23]. To account for the variability of the density and Poisson ratio across different components of the model, a range of 25% was set as the upper and lower bounds for these parameters. But these bounds were not considered for the elastic modulus values.

Table 1
The ADF and MAC values of SSI and fixed-base models after calibration.

Model type	FEA Mode	Frequency (Hz)	OMA Mode	Frequency (Hz)	ADF (%)	MAC (%)
SSI model	1	8.343	1	8.007	4.19	71.7
	2	10.462	2	10.22	2.28	66.4
	4	11.222	3	11.206	0.14	70.5
	16	14.926	4	16.357	8.75	60.1
Fixed-base model	1	8.458	1	8.007	5.62	70.4
	2	10.897	2	10.229	6.53	67.2
	3	11.586	3	11.206	3.39	70

The absolute difference in natural frequency (ADF) and MAC values of both models is presented in Table 1. The MAC matrices and the correlated mode shapes are presented in Fig. 8 for both models. The bridge was calibrated with a minimum MAC of 60.1% for all four modes of the SSI model. But the fixed-base model could not be correlated to the test results for the fourth mode. Considering the SSI effects that increase the number of parameters, the SSI model has a better correlation with OMA results compared to the fixed-base model. The MAC matrix of the SSI model shows some predominantly soil-contributed modes that can be defined by investigating the mass participation vectors. Therefore, the four first dominant structure modes were paired with the OMA modes in order.

The updated E of each bridge portion is illustrated in Fig. 9 (a). The erosion of the central pier detected through the visual inspection is reported in Fig. 9 (a) by checking the E values of this part, which are relatively low compared to the other masonry parts. Note that the indices R, L, and C represent the location of the section, considering that the left side is the side closest to the stream bed. The terms B and F denote the back and front sides, as illustrated in Fig. 9 (b). The calibrated E values of the central, left, and right foundations are 852.189, 958.79, and 1012.6 MPa, respectively, and the soil elastic modulus is 5470 MPa. The E values of the backfill soil are increased by 55% and 78% for SSI and fixed-base models, respectively, showing that the initial assumption underestimates the stiffness of this part. The updated material properties of each component of both bridge models are presented in Tables A1 and A2 in the appendix.

3.7. Nonlinear model development

The first step towards performing a robust enough seismic evaluation methodology is to define proper nonlinear material behavior. In this light, the total strain-based crack model was utilized to represent the nonlinear behavior of the stone masonry part [47]. Note that the maximum compressive strength of each part was computed as 0.2% of the E value, and the maximum tensile strength was calculated as 15% of the compressive strength based on the empirical rules presented in [56,57]. The fracture energy in compression and tension would be calculated as 1.6 and 0.029 times the maximum compressive strength [56,57]. Fig. 10 depicts the stress–strain curves of the total strain-based crack model. Note that the area under the exponential softening curve is calculated based on the tension fracture energy divided by the definition of the crack bandwidth (h) of an element [47]. For the compression part, the area under the parabolic curve is calculated based on the

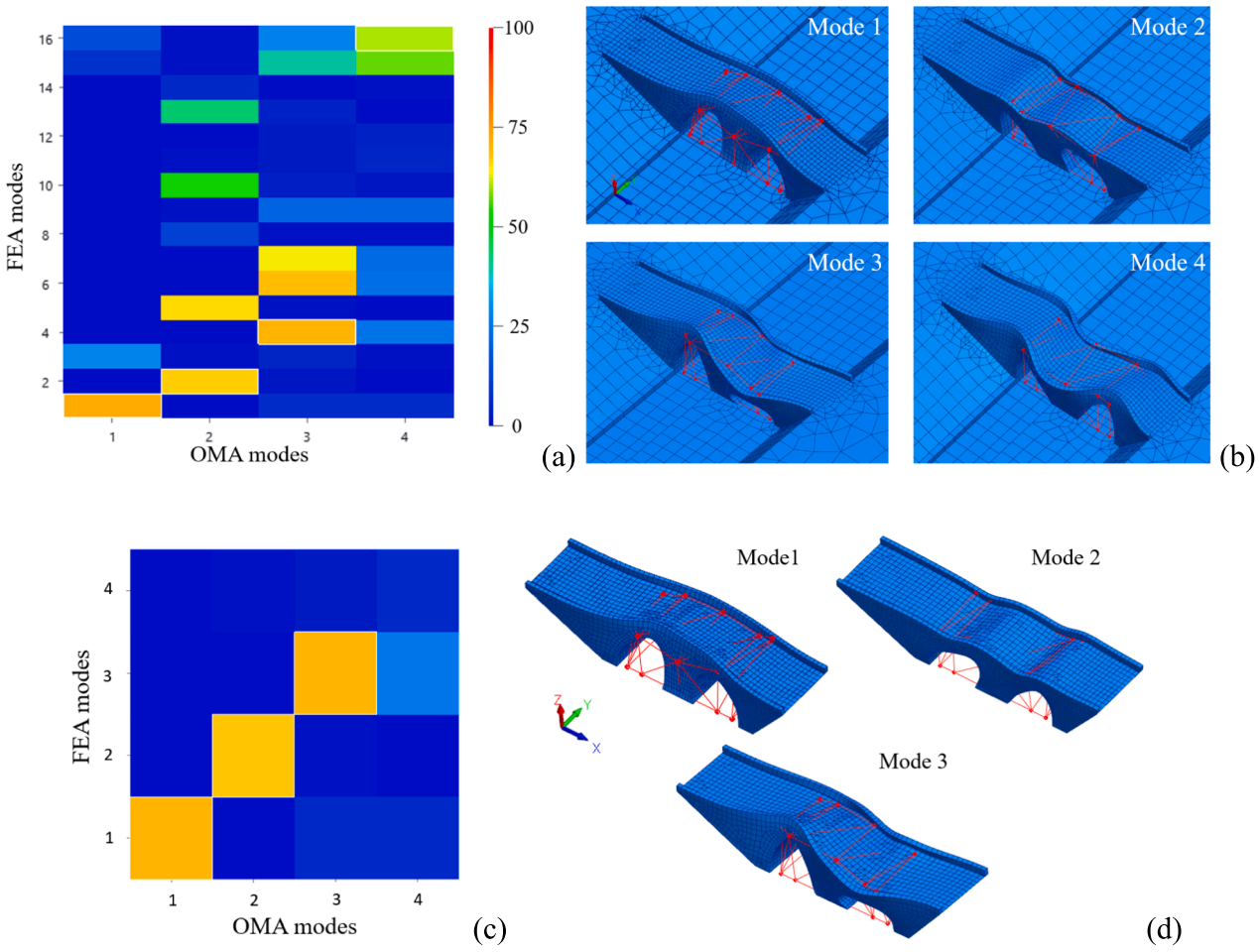

Fig. 8. (a) MAC matrix and (b) mode shape correlations of the SSI model, (c) MAC matrix, and (d) mode shape correlations of the fixed-base model.

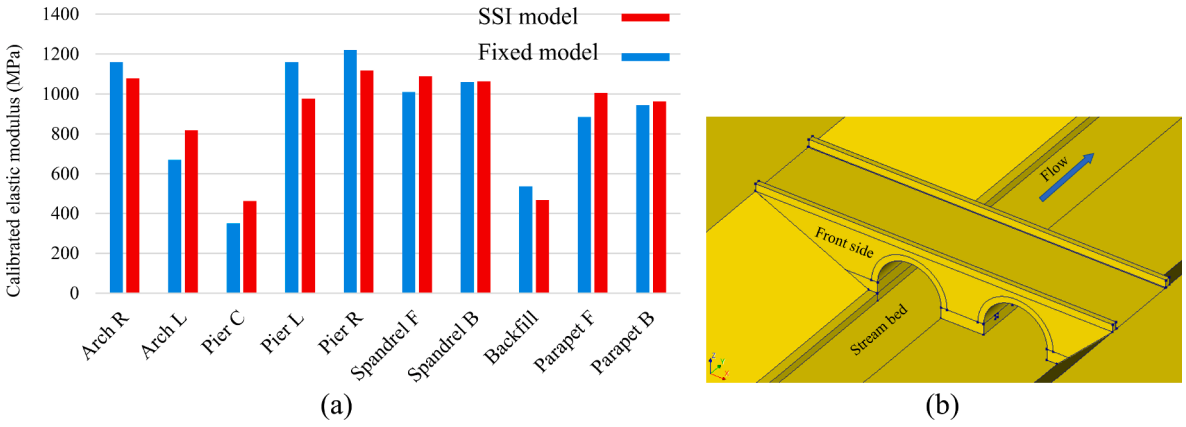

Fig. 9. (a) Updated E values of different parts of the SSI and fixed-base models and (b) stream bed location and the front side of the bridge model.

compression fracture energy divided by h to define the stress–strain curve of the masonry. The shear capacity of the masonry part decreases to zero until the part is sufficiently damaged. The mechanical properties of each bridge component were calculated and presented in the appended Tables A1 and A2. The Mohr-Coulomb material model, which is a simpler material model than the total strain crack model, was chosen to simulate the backfill soil behavior with a cohesion of 0.05 MPa, a friction angle of 0.35 rad, and maximum tensile strength of 0.05 MPa [64].

The soil is simulated based on the Hardin-Drnevich material model, an elastic model with a nonlinear shear stress-shear strain relationship [65]. In the Hardin-Drnevich model, the relationship between shear stress and shear strain is defined by:

$$\tau = \frac{G_{max}\gamma}{1+\frac{\gamma}{\gamma_r}} \tag{5}$$

where γ and γ_r are shear strain and characteristic shear strain of the soil, and G_{max} is the maximum shear modulus calculated based on:

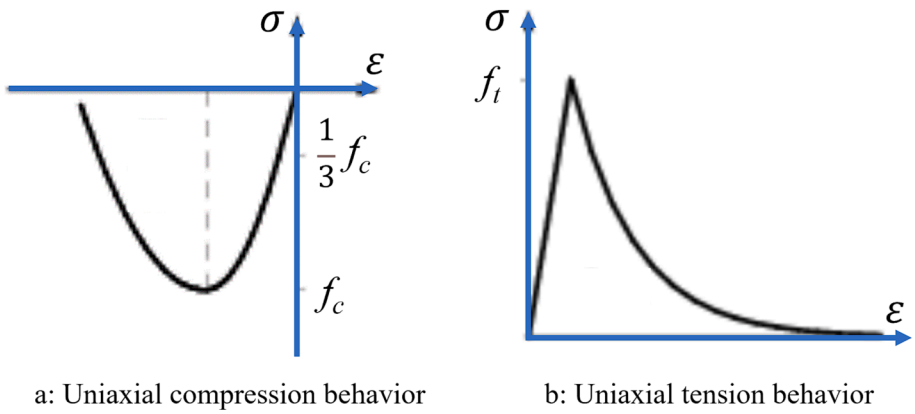

Fig. 10. Stress–strain diagrams of the homogenized stone masonry based on the total strain-based crack for (a) tension and (b) compression.

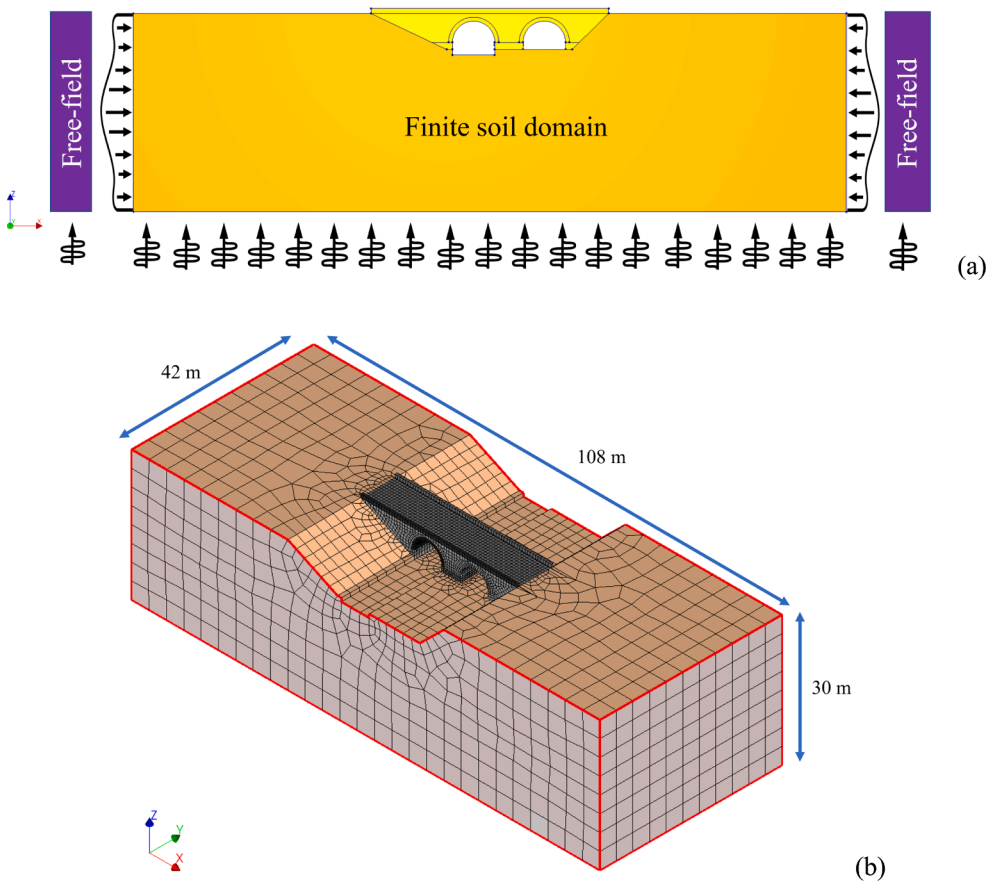

Fig. 11. (a) Schematic representation of the free-field elements and (b) dimension of the SSI model with free-field boundary elements.

$$G_{max} = \frac{E}{2(1+\vartheta)} \tag{6}$$

where ϑ is the Poisson ratio of soil. γ_r was considered 0.0015 for the surrounding soil based on [65].

In geotechnical dynamic problems, considering either rigid or free boundary conditions for the soil leads to unrealistic results. Furthermore, the very large soil domain considered for the SSI model in this study is another strategy that leads to high computational effort for performing nonlinear dynamic analysis. To tackle these limitations, free-field boundary conditions can be utilized by decreasing the size of the soil part. The free-field motions around the soil part are converted into boundary tractions applied to the finite soil part. The free field affects the behavior of the main model, not vice versa. Furthermore, the free-field elements have dashpots to absorb the outgoing waves, which causes unrealistic effects on the main model using rigid boundary conditions [66,67]. Fig. 11 (a) illustrates the schematic representation of the free-field boundary element where compressive loads are applied to the finite soil domain as an example. A new model with dimensions more than three times those of the bridge in the corresponding direction was developed, and free-field elements were assigned to the four sides of the finite soil domain [18]. Note that rigid boundary conditions were applied to the bottom face. The SSI model with free-field elements with dimensions is depicted in Fig. 11 (b). The SSI model with free-field elements was only utilized for performing nonlinear dynamic analysis.

Table 2
Quantitative and qualitative description of three performance levels of masonry arch bridges.

Performance level	Functionality (F)	Life safety (LS)	Near collapse (NC)
Quantitative description	Displacement corresponds to 75% of the maximum base shear (or acceleration)	Displacement corresponds to the first point on the pushover curve with a tangential stiffness equals to 7% of the initial (elastic) stiffness	Displacement corresponds to 90% of the maximum displacement attained on the pushover curve
Qualitative description	Structure is mostly elastic with little or no damage. Traffic is not interrupted, and damage can be repaired in a couple of days	Plasticity starts increasing before and after this performance level. The bridge is expected to suffer medium to significant damage. Still, it should be feasible to repair but cannot be used for a short duration	The damage is heavy and distributed to the extent that the bridge is near to collapse state. The bridge may even be out-of-service or replaced completely

4. Seismic analysis

4.1. Pushover analysis and defining limit states

A predefined performance limit state definition for seismic assessment of masonry bridges in the transverse direction is not available. Thus, a structure-specific methodology based on the nonlinear pushover curve is followed to define the Roman bridge's limit states [68]. In this light, the three performance levels are defined and qualitatively presented in Table 2, and the method for defining the limit state values based on the displacement values of the crown points is elaborated in Table 2. The relationship between performance levels and damage states is shown in Fig. 12 (a). A modal pushover analysis was performed with a load pattern based on the first mode shape, and the pushover curve in terms of displacement of the node between two arches in the parapet element (crown point) versus base shear is plotted in Fig. 12 (b). The limit states are calculated and illustrated in Fig. 12 (b), which are 3.784 mm, 4.983 mm, and 8.387 mm for functionality (F), life safety (LS), and near collapse (NC) limit states, respectively.

4.2. Seismic record selection

Probabilistic seismic hazard analysis (PSHA) is performed based on the SHARE area source model [69] for the bridge site located at

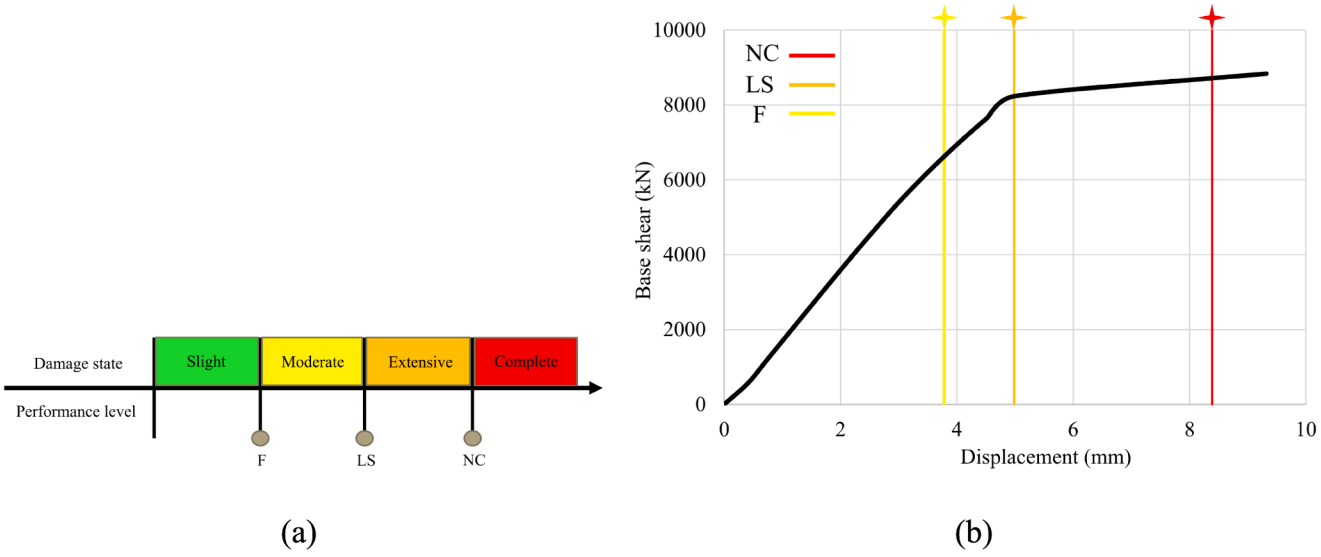

Fig. 12. (a) Relationships between performance levels and damage states, and (b) pushover curve and performance limits of the Roman bridge.

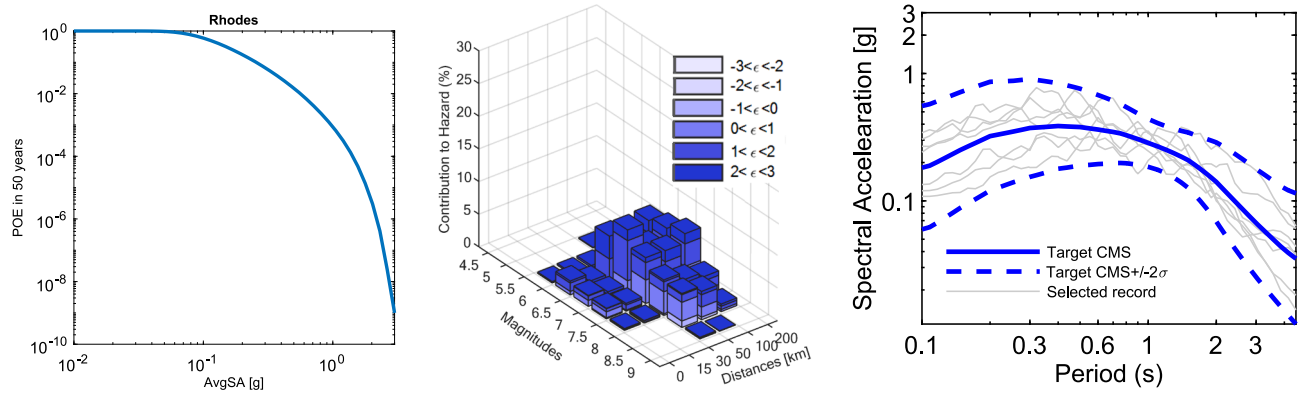

Fig. 13. (a) Hazard curve for AvgSA, (b) Disaggregation of the hazard, and (c) selected records based on the CS record selection approach for the 10% probability of exceedance in 50 years.

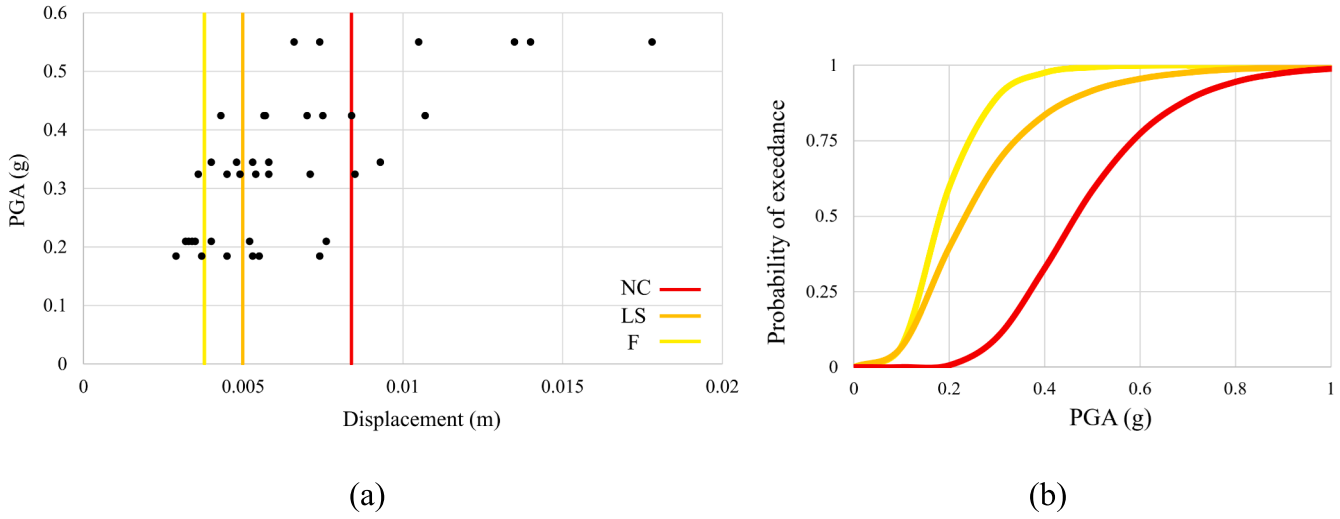

Fig. 14. (a) MSA results with performance limit values and (b) seismic fragility curves of the case study.

coordinates 28.219°E, 36.439°N. It is assumed that the bridge is located on hard soil with a 600 m/s average shear wave velocity for the top 30 m of the soil (V_{s30}) consistent with the hard soil, which was assumed in the model updating process. The ground motion prediction equation (GMPE) proposed by Boore and Atkinson is used for all purposes of this study, considering all the seismic sources within 200 km of the site [70]. Fig. 13 (a) illustrates the hazard curve at the selected site based on the average spectral acceleration (AvgSA) in the period range of [0.2, 2.0] s with a 0.1 s increment. OpenQuake [71], an open-source software for seismic hazard and risk assessment developed by the Global Earthquake Model Foundation, is used to perform the seismic hazard and disaggregation computations of this study. Fig. 13 (b) shows the disaggregation of the hazard for a 10% probability of exceedance in 50 years.

Five suites of records for five IM levels corresponding to 10.0%, 2.0%, 1.0%, 0.6%, and 0.2% probability of exceedance in 50 years were selected and scaled based on the conditional spectrum (CS)-based method [72]. At each IM level, seven pairs of records from the NGA-West database [73] were selected to match the target spectrum. The selection is based on the approximate method of CS using the mean scenarios from the hazard [74]. Fig. 13 (c) depicts the conditional mean spectrum (CMS) of the seven records selected for the IM level with a 10% probability of exceedance in 50 years as a sample.

In this study, each record was scaled to the median PGA value of its IM records due to the simplicity of using the term PGA instead of AvgSA. This assumption is consistent with the project goal, which is the large-scale seismic assessment of the Rhodes and maintains the hazard consistency of the site.

4.3. MSA and seismic fragility curves

The MSA method is based on the assumption that the response of a structure can be approximated as a series of intervals, or "stripes," each

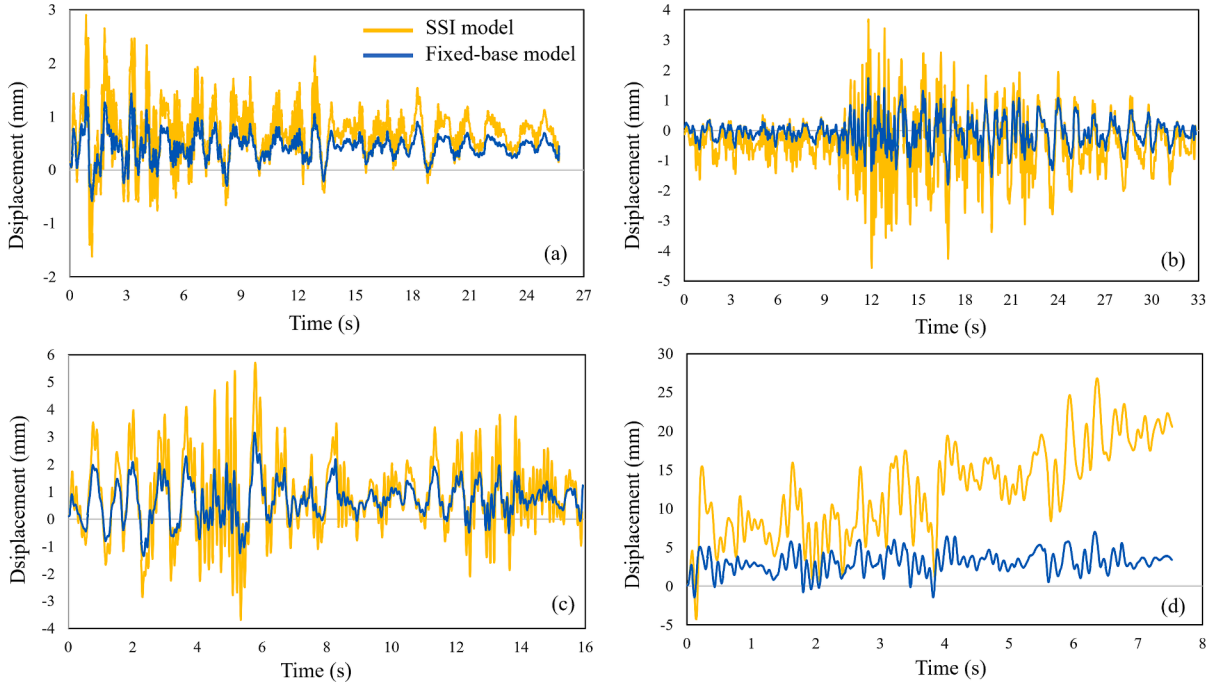

Fig. 15. Displacement response time history of the crown nodes of the models subjected to the seismic records that impose (a) slight, (b) moderate, (c) extensive damages, and (d) complete collapse to the SSI model.

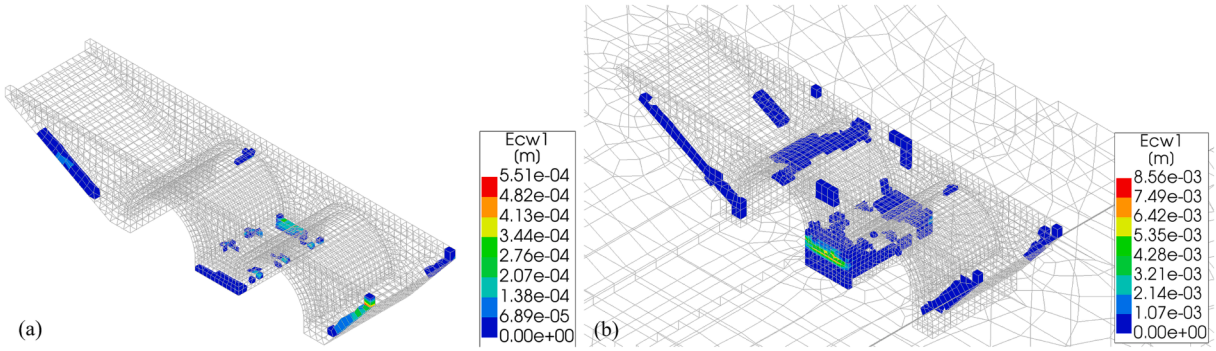

Fig. 16. Crack pattern and width of (a) fixed-base and (b) SSI models subjected to the seismic record that imposed extensive damages to the SSI model.

of which is characterized by a different ground motion intensity level [40]. By means of MSA, the performance of a structure is evaluated under a range of ground motion intensities, from relatively weak events to very strong events, which allows engineers to identify vulnerabilities and develop effective strategies for reducing earthquake risk.

The PGA values of the five seismic record sets were scaled to the PGA values of the selected seismic records based on the CS approach. However, to apply stronger ground motions to evaluate the structure in the complete collapse damage state, the last two record sets with IM levels of 4 and 5 were scaled to PGA, 0.55 g, and 0.67 g, respectively. Therefore, seven groups of records with seven PGA values were applied to the SSI model with free-field boundary conditions, and MSA was carried out [40] considering 5% of the Rayleigh damping ratio for the first and third natural modes in the transverse direction [75]. Note that for the sake of decreasing the level of computational effort, each seismic record was applied to the bridge during the excitation's significant duration.

Fig. 14 (a) illustrates the maximum crown displacement values versus PGA values of each stripe and the three calculated limit states. The crack pattern and width of the models reveal that the central pier is the most critical structural component, and the arches are the second most susceptible members.

The fragility curves' parameters were estimated by maximizing a likelihood function. In other words, the distribution derived from the parameters has the highest likelihood of having produced the observed data from the MSA [41]. The fragility curves were produced for the three limit states and are illustrated in Fig. 14 (b). The probability of complete collapse of the bridge subjected to seismic records with PGA greater than 0.46 g is more than 50%. The results from the fragility curves can be utilized for post-earthquake management strategies at a building or large scale.

4.4. The effect of SSI on the seismic behavior

The effect of SSI on the seismic behavior of the bridge is investigated by comparing the results of the nonlinear time history analysis of the two calibrated models. In this light, four seismic excitations were chosen that impose slight, moderate, and extensive damages and complete collapse with PGA values of 0.18 g, 0.32 g, 0.42 g, and 0.55 g, respectively, based on the MSA. The seismic records were applied to the models to highlight the displacement differences, as illustrated in Fig. 15. The differences are not inevitable, which is drastically high for the ground motion with the highest PGA.

The numerical models at the end of the nonlinear time history analysis that impose extensive damage to the bridge with crack patterns are shown in Fig. 16 as an example. The maximum crack width of the SSI model is 15.5 times bigger than that of the fixed base model. Furthermore, the cracks are limited to the bridge's central pier in the fixed-base model, but in the SSI model, more cracks can be detected in the central pier and the left arch. Therefore, the fixed-base models dangerously underestimate the seismic behavior of masonry bridges in the transverse direction.

Table 3
Material properties of the enhanced stone masonry.

Parameter	Value for the enhanced masonry
Compressive strength (MPa)	3.539
Tensile strength (MPa)	0.531
Elastic modulus (MPa)	1769.5
Fracture energy in compression (for the f_c lower than 12 MPa) (N/mm)	5.662
Fracture energy in tension (N/mm)	0.015

5. Seismic strengthening proposals

The model calibration, the seismic analyses, and the visual inspection show that the central pier and the aches are the most susceptible structural elements of the Roman bridge. Hence, three strengthening strategies are proposed to ensure the bridge's safety during seismic events.

The first strengthening strategy involves removing the backfill and enhancing the arches by replacing the existing stone masonry with Sfouggaria stones with a compressive strength of 9 MPa. The stones would be mounted and connected via lime mortar with a punch test of less than 20 mm and a compressive strength of 4 MPa. The same stone would be chosen to maintain the consistency of the structure. To strengthen the central pier, the vegetation around it would be removed, and the stones around the pier would be replaced and connected via lime mortar with a depth of 0.5 m. Finally, the backfill would be refilled. A FE model labeled "newmat" was developed by modifying the material properties of the arches and the central pier. The compressive strength of the enhanced masonry was calculated as 3.539 MPa based on the mechanical properties of the stone and mortar using Equation (1) [56,57]. The tensile strength was considered 15% of the compressive strength [1], and the elastic modulus, fracture energy in compression, and tension were considered 500, 1.6, and 0.029 times the compressive strength, as suggested in [56,57]. Table 3 shows the material properties of the enhanced stone masonry.

Replacing the stone masonry of the arch and central pier keeps the consistency and respects the authenticity of this historic infrastructure by using the same material. Strengthening the arches with the improved masonry material, like the first strategy, and strengthening the central pier using fiber-reinforced concrete mortar (FRCM) is another strengthening strategy. Strengthening the pier with FRCM systems can be less challenging and more cost-effective than replacing the existing material with improved stone masonry material. Furthermore, low maintenance and high durability are advantages of using FRCM systems for strengthening purposes [76]. However, the texture of the central pier would be changed, and FRCM systems are not in harmony with stone masonry in terms of mechanical properties.

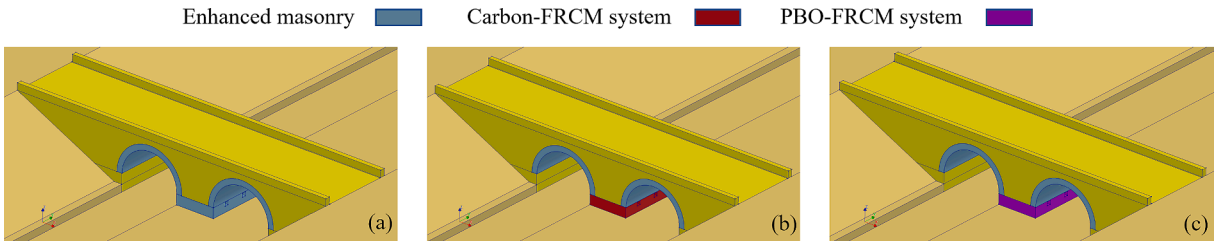

Fig. 17. (a) Newmat and (b) Carbon-FRCM and (c) PBO-FRCM numerical models.

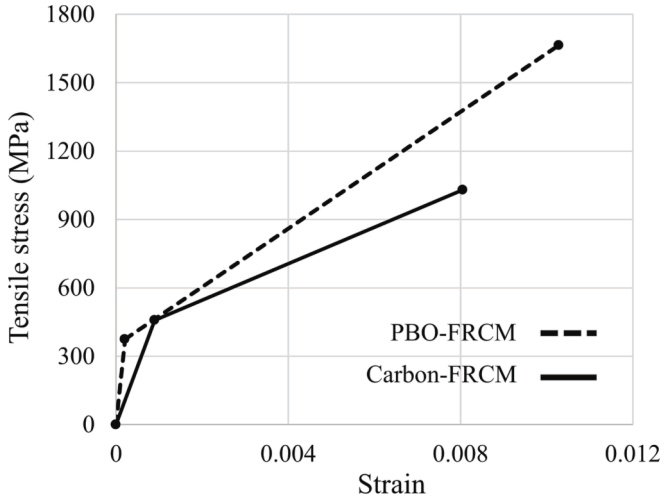

Fig. 18. The stress–strain curve of FRCM systems in tension.

The third strategy involves strengthening the arches with improved masonry material and using a FRCM system to strengthen the central pier. Polyparaphenylene benzobisoxazole (PBO) and carbon FRCM systems [77,78] could be the potential FRCM systems for strengthening the pier element. For this aim, two FE models were made by modeling the Carbon-FRCM and PBO-FRCM layers covering the central pier with a thickness of 0.05 m, as depicted in Fig. 17 (b) and (c).

The phenomenological laws of the FRCM systems associated with the tensile stress–strain curves are presented in Fig. 18 based on [79]. The idealized tensile stress–strain curve is initially linear until the cracking of the cementitious matrix. Then the curve continues until the ultimate capacity. Fig. 18 shows that the elastic modulus maximum tensile strength of PBO-FRCM is larger than that of the carbon-FRCM system. However, the cracking of the cementitious matrix happens sooner in PBO-FRCM systems than in carbon-FRCM systems.

Debonding between FRCM layers and masonry is less probable [80,81]. Therefore, as a simplified assumption, a perfect bond between the FRCM layers and the masonry was assumed in the numerical models [32,78,82]. Modal analysis was performed. The fundamental frequencies of the newmat, PBO-FRCM, and carbon-FRCM models are 10.014 Hz, 10.598 Hz, and 10.554 Hz, respectively. Therefore, the elastic stiffness of the strengthened models is increased by 25%, 32.3%, and 31.8%, respectively.

5.1. Seismic response of the strengthened models

The seismic response of the strengthened models was evaluated by updating the Rayleigh damping factors of the three models to account for changes in their modal properties. The excitations that impose the median displacement demand of the last three stripes were chosen as records (a), (b), and (c) with PGA values of 0.42 g, 0.55 g, and 0.66 g. Record (a) imposes extensive damage to the existing structure excitations, while the other two records force complete collapse.

The excitations were applied to the three strengthened models. The crown displacement time history responses of the three strengthened models and the existing structure model subjected to the three selected seismic excitations are presented in Fig. 19. The displacement time history of the strengthened models showed negligible differences, indicating that the strengthening strategies had effectively improved the seismic behavior of the bridge. Fig. 19 (d) shows the models' maximum displacements, highlighting the improvement in seismic performance.

The results revealed that the efficiency of the strengthening models increased with more intensive seismic excitations. The PBO-FRCM system was found to be the best model with the least maximum displacement among the strengthening models. The differences between the maximum displacements of the PBO- and carbon-FRCM models were negligible. These findings demonstrate the proposed strengthening methods' efficacy in enhancing the bridge's seismic resistance, particularly when subjected to high-intensity seismic events.

The crack patterns and widths of the models were analyzed to assess the effectiveness of the strengthening strategies. The crack patterns and the crack widths of the models are plotted in Fig. 20. The results reveal that cracks would disappear in arches by enhancing the mechanical properties of the masonry part of the arches. The maximum crack width is decreased for all strengthened models, which is significant for the higher intensities, which are records (b) and (c).

The crack patterns in both FRCM-strengthened models were limited to the region between the masonry pier covered with FRCM and the upper part. Cracks with a width of less than 2 mm were observed in this region due to the high stiffness difference between the upper masonry part and the strengthened pier. On the other hand, the cracks in the existing structure model and the newmat model were concentrated in the middle of the central pier.

The crack width of the newmat model was lower than the FRCM-strengthened models subjected to the record (a), with the lowest intensity due to the material consistency. However, with increasing excitation intensities, the crack width of the FRCM models was lower than the newmat model. Among the FRCM-strengthened models, the PBO-FRCM model exhibited the lowest crack width, and differences between the crack widths of the FRCM-strengthened models were not negligible.

Considering the Roman bridge's significance as a cultural heritage asset, enhancing the mechanical properties of the masonry material of the central pier and the arches would be the most appropriate strengthening strategy. This strategy would harmonize with the existing structure, and discontinuities in mechanical properties would not appear. However, employing FRCM systems for strengthening the central pier would change the bridge's texture and appearance. Despite this, the results of the crack width analysis for models subjected to more substantial ground motions demonstrate the effectiveness of these systems in enhancing the bridge's seismic performance.

The results of this part of the study have significant implications for the maintenance and preservation of historic masonry structures such as the Roman bridge. By evaluating and comparing the performance of different strengthening strategies under seismic loads, the study provides valuable insights for engineers and conservationists seeking to ensure the long-term structural stability and safety of such heritage

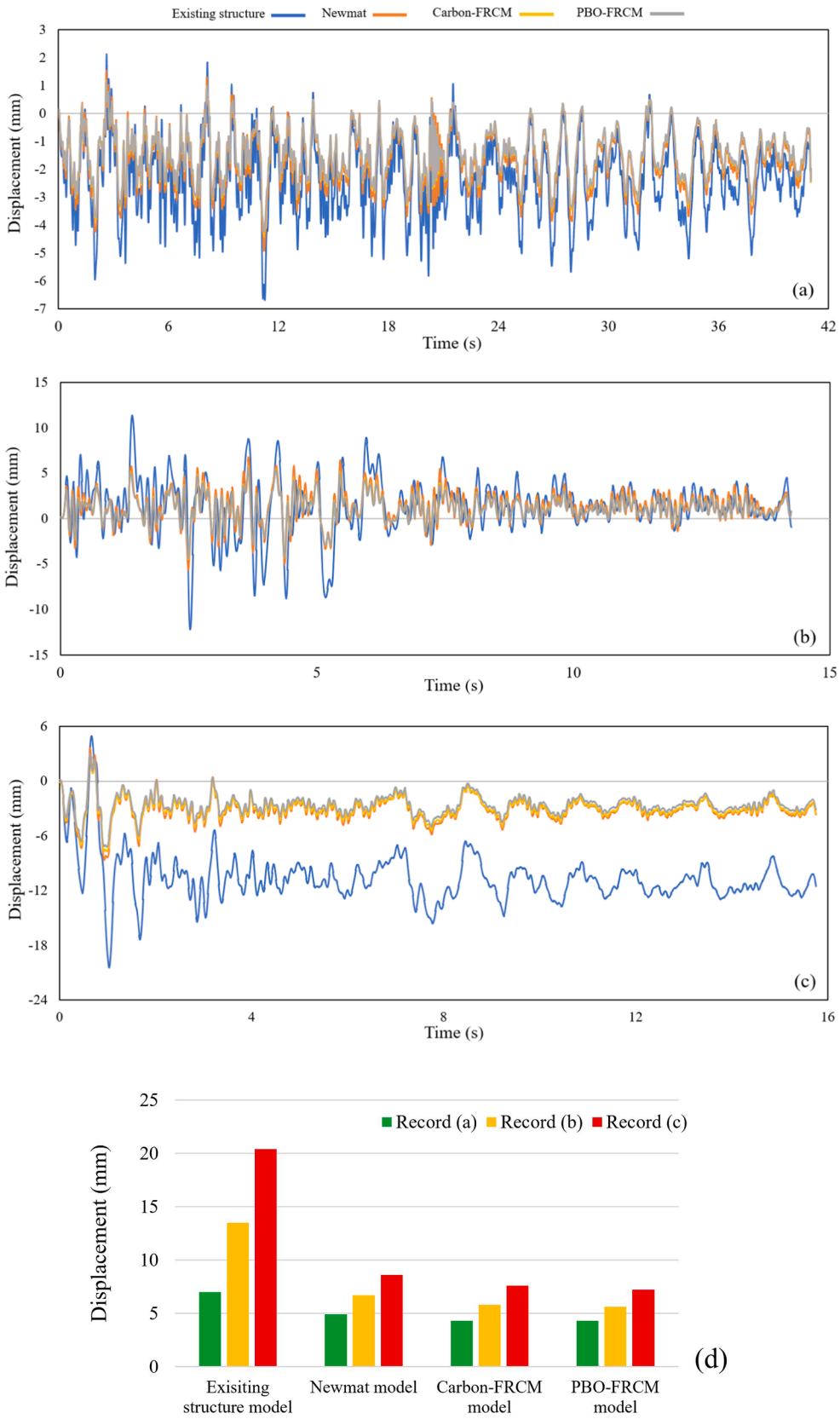

Fig. 19. Displacement time history response of the crown nodes of the SSI and strengthened models subjected to record (a), (b), (c), and (d) maximum displacement values.

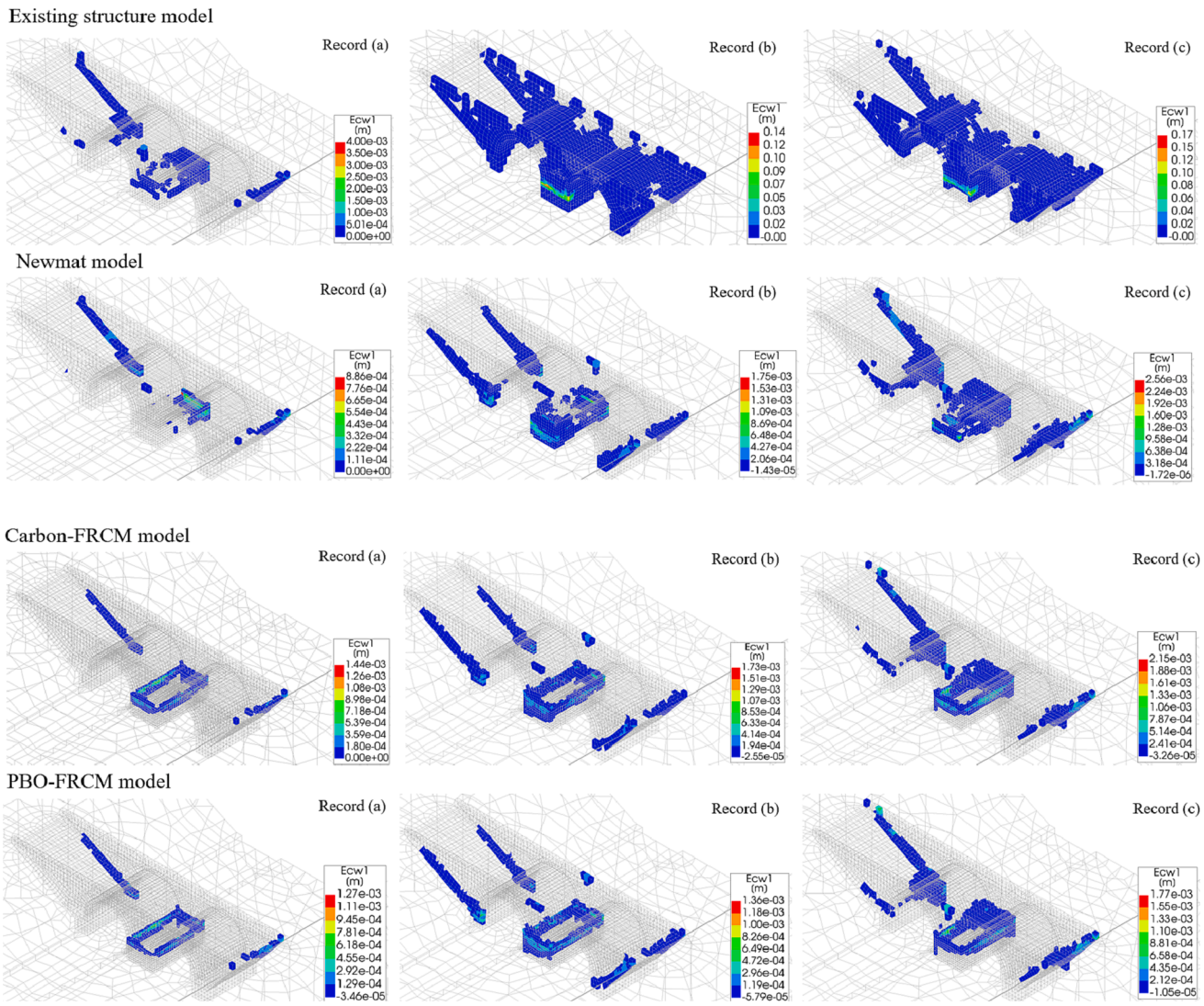

Fig. 20. Crack patterns and width values of the existing structure model and strengthened models subjected to the three chosen seismic excitations.

assets. The findings suggest that using FRCM systems can effectively enhance the seismic resistance of masonry arch bridges without compromising their aesthetic and historical value. However, selecting the most suitable strengthening strategy should be based on a comprehensive assessment of the bridge's existing condition, structural characteristics, and historical significance. In conclusion, this study highlights the importance of a multidisciplinary and collaborative approach to the conservation of cultural heritage structures, considering both technical and cultural aspects.

6. Conclusions

This paper presented a methodology composed of two main steps: geometric documentation and model calibration, resulting in the 3D nonlinear model of a historical stone masonry bridge. Afterward, MSA is performed to define the fragility curves of the case study for three performance levels. Note that two models, SSI and fixed-base models with and without SSI, were developed. Both models were calibrated based on the OMA results. After determining the susceptible parts of the bridge through visual inspection, model calibration, and seismic analysis, three strengthening strategies were proposed, and three models were developed. In the newmat model, the mechanical properties of the masonry of the central pier and arches are improved using Sfouggaria stone and a firmer lime mortar. In the PBO and Carbon–FRCM models, the arches are strengthened using improved masonry, but the central pier is covered with the mentioned FRCM systems.

- The calibration of the models confirms the structural damages to the central pier and arches of the bridge detected based on the visual inspection. The MSA of the SSI model with free-field boundary elements reveals that the damages to the susceptible part are worsened by increasing the seismic intensities.
- Seismic fragility curves are helpful for management strategies and post-earthquake loss estimation at a single structure or on a large scale. The fragility curves of the SSI model show that the probability of complete collapse of the bridge subjected to seismic records with PGA greater than 0.46 g is more than 50%.
- The seismic behavior of SSI and fixed-base models in terms of displacement, crack pattern, and crack width shows that neglecting the SSI effects underestimates the seismic behavior of masonry bridges in the transverse direction.
- A comparative study of the seismic response of the strengthened bridge models subjected to three seismic records reveals that the newmat model would be the best strengthening strategy that improves the seismic behavior of the bridge and satisfies the criteria concerning the strengthening of historic structures. Compared to using FRCM systems to cover and strengthen the central pier, the strengthening strategy with improved masonry keeps the consistency

Table A1
Updated material properties of the SSI model.

Component name	E (MPa)	ρ (kg/m^3)	ϑ	f_c(MPa)	f_t(MPa)	g_{f_c} (N/mm)	g_{f_t} (N/mm)
Arch R	1078.39	1936.39	0.297	2.158	0.323	3.451	0.009
Arch L	818.393	2750	0.291	1.637	0.245	2.619	0.007
Soil	5470.21	1809.92	0.306				
Pier C	462.414	2243.91	0.285	0.925	0.139	1.479	0.004
Pier L	977.554	2195.7	0.302	1.955	0.293	3.128	0.008
Pier R	1118.09	2051.42	0.296	2.236	0.335	3.578	0.009
Spandrel F	1088.86	2192.93	0.306	2.178	0.327	3.484	0.009
Spandrel B	1064.6	2103.73	0.307	2.129	0.319	3.407	0.009
Backfill	466.463	2408.02	0.250				
Foundation C	852.189	2208.05	0.276	1.704	0.256	2.728	0.007
Foundation L	985.79	2200.87	0.3	1.971	0.296	3.154	0.008
Foundation R	1012.6	2200.11	0.301	2.025	0.304	3.24	0.009
Parapet F	1005.45	2093.24	0.3	2.011	0.302	3.217	0.009
Parapet B	963.146	2037.97	0.3	1.926	0.289	3.082	0.008

Table A2
Updated material properties of the fixed-base model.

Component name	E (MPa)	ρ (kg/m^3)	ϑ	f_c(MPa)	f_t(MPa)	g_{f_c} (N/mm)	g_{f_t} (N/mm)
Arch R	1158.35	1650	0.258	2.317	0.348	3.707	0.01
Arch L	670.37	2750	0.263	1.341	0.201	2.145	0.006
Pier C	350.35	2243.93	0.286	0.701	0.105	1.121	0.003
Pier L	1158.27	2193.84	0.299	2.317	0.347	3.706	0.01
Pier R	1222.97	2194.24	0.304	2.446	0.367	3.914	0.011
Spandrel F	1008.29	1980.5	0.306	2.017	0.302	3.227	0.009
Spandrel B	1057.31	1838.88	0.300	2.115	0.317	3.383	0.009
Backfill	534.967	2750	0.225	1.070	0.160	1.712	0.005
Parapet F	884.337	1913.03	0.301	1.769	0.265	2.830	0.008
Parapet B	944.662	1895.6	0.300	1.889	0.283	3.023	0.008

of the structure in harmony with other parts of the bridge without increasing the stiffness significantly and respecting the originality of the historic structure.
- However, FRCM systems can be more cost-effective, durable, and resilient when the structure is subjected to strong ground motions than the improved masonry strategy. The PBO-FRCM system is more effective than the carbon-FRCM system in terms of crack width for strengthening the central pier, although the differences in maximum displacement responses of the crown nodes are negligible.

It is emphasized that, in this paper, a linear material model was considered for the soil part with nonlinear shear stress–strain behavior. Therefore, seismic analysis of the bridge with free-field elements and a nonlinear material model for the soil part would be a future study. An on-site test for investigating the mechanical properties of the soil will improve the authenticity of the work and decrease the uncertainty level of the study. Furthermore, predefined limit state definitions should be defined and presented in seismic assessment codes by performing nonlinear pushover analysis of masonry arch bridges in the transverse direction with different geometries and material properties.

CRediT authorship contribution statement

Amirhosein Shabani: Conceptualization, Methodology, Software, Validation, Formal analysis, Investigation, Resources, Data curation, Writing – original draft, Writing – review & editing, Visualization.

Mahdi Kioumarsi: Methodology, Investigation, Resources, Writing – review & editing, Visualization, Supervision, Project administration, Funding acquisition.

Declaration of Competing Interest

The authors declare that they have no known competing financial interests or personal relationships that could have appeared to influence the work reported in this paper.

Data availability

The authors do not have permission to share data.

Acknowledgments

This work is a part of the HYPERION project. HYPERION has received funding from the European Union's Framework Programme for Research and Innovation (Horizon 2020) under grant agreement no. 821054. The contents of this publication are the sole responsibility of Oslo Metropolitan University (Work Package 5, Task 2) and do not necessarily reflect the opinion of the European Union. The authors appreciate the comment and supervision of Dr. Dimitrios Vamvatsikos and Dr. Mohsen Kohrangi concerning the seismic record selection and analysis sections. We thank the Ephorate of Antiquities of the Dodecanese for their assistance during the tests.

Appendix A. Calibrated material properties

In this appendix, the calibrated material properties of different components of the bridge are presented for SSI and fixed-base models. Note that E, ρ, g_{f_c}, g_{f_t} refer to the elastic modulus, density, fracture energy in compression, and fracture energy in tension, respectively.
Tables A1 and A2

References

[1] Gönen S, Soyöz S. Seismic analysis of a masonry arch bridge using multiple methodologies. Eng Struct 2021;226:111354. https://doi.org/10.1016/j.engstruct.2020.111354.

[2] Sarhosis V, De Santis S, de Felice G. A review of experimental investigations and assessment methods for masonry arch bridges. Struct Infrastruct Eng 2016;12:1439–64. https://doi.org/10.1080/15732479.2015.1136655.

[3] Helmerich R, Niederleithinger E, Trela C, Bień J, Kamiński T, Bernardini G. Multi-tool inspection and numerical analysis of an old masonry arch bridge. Struct Infrastruct Eng 2012;8:27–39. https://doi.org/10.1080/15732471003645666.

[4] de Felice G. Assessment of the load-carrying capacity of multi-span masonry arch bridges using fibre beam elements. Eng Struct 2009;31:1634–47.

[5] Audenaert A, Fanning P, Sobczak L, Peremans H. 2-D analysis of arch bridges using an elasto-plastic material model. Eng Struct 2008;30:845–55.

[6] Pantò B, Grosman S, Macorini L, Izzuddin BA. A macro-modelling continuum approach with embedded discontinuities for the assessment of masonry arch bridges under earthquake loading. Eng Struct 2022;269:114722. https://doi.org/10.1016/j.engstruct.2022.114722.

[7] Papa T, Grillanda N, Milani G. Three-dimensional adaptive limit analysis of masonry arch bridges interacting with the backfill. Eng Struct 2021;248:113189. https://doi.org/10.1016/j.engstruct.2021.113189.

[8] Lemos JV. Discrete Element Modeling of Masonry Structures. International Journal of Architectural Heritage 2007;1:190–213. https://doi.org/10.1080/15583050601176868.

[9] Saygılı Ö, Lemos JV. Seismic vulnerability assessment of masonry arch bridges. Structures 2021;33:3311–23. https://doi.org/10.1016/j.istruc.2021.06.057.

[10] Milani G, Lourenço PB. 3D non-linear behavior of masonry arch bridges. Comput Struct 2012;110:133–50.

[11] D'Altri AM, Sarhosis V, Milani G, Rots J, Cattari S, Lagomarsino S, et al. Modeling Strategies for the Computational Analysis of Unreinforced Masonry Structures: Review and Classification. Arch Comput Meth Eng 2020;27:1153–85. https://doi.org/10.1007/s11831-019-09351-x.

[12] Reccia E, Milani G, Cecchi A, Tralli A. Full 3D homogenization approach to investigate the behavior of masonry arch bridges: The Venice trans-lagoon railway bridge. Constr Build Mater 2014;66:567–86. https://doi.org/10.1016/j.conbuildmat.2014.05.096.

[13] Zampieri P, Tetougueni CD, Pellegrino C. Nonlinear seismic analysis of masonry bridges under multiple geometric and material considerations: Application to an existing seven-span arch bridge. Structures 2021;34:78–94. https://doi.org/10.1016/j.istruc.2021.07.009.

[14] Simos N, Manos GC, Kozikopoulos E. Near- and far-field earthquake damage study of the Konitsa stone arch bridge. Eng Struct 2018;177:256–67. https://doi.org/10.1016/j.engstruct.2018.09.072.

[15] Anand V, Satish Kumar SR. Seismic Soil-structure Interaction: A State-of-the-Art Review. Structures 2018;16:317–26. https://doi.org/10.1016/j.istruc.2018.10.009.

[16] Zani G, Martinelli P, Galli A, di Prisco M. Three-dimensional modelling of a multi-span masonry arch bridge: Influence of soil compressibility on the structural response under vertical static loads. Eng Struct 2020;221:110998. https://doi.org/10.1016/j.engstruct.2020.110998.

[17] Güllü H, Özel F. Microtremor measurements and 3D dynamic soil–structure interaction analysis for a historical masonry arch bridge under the effects of near- and far-fault earthquakes. Environ Earth Sci 2020;79:338. https://doi.org/10.1007/s12665-020-09086-0.

[18] Bayraktar A, Hökelekli E. Nonlinear soil deformability effects on the seismic damage mechanisms of brick and stone masonry arch bridges. Int J Damage Mech 2021;30:431–52. https://doi.org/10.1177/1056789520974423.

[19] Zani G, Martinelli P, Galli A, Gentile C, Prisco Md. Seismic Assessment of a 14th-Century Stone Arch Bridge: Role of Soil–Structure Interaction. Journal of Bridge Engineering, 2019.24:05019008, doi:10.1061/(ASCE)BE.1943-5592.0001441.

[20] Angjeliu G, Coronelli D, Cardani G. Development of the simulation model for Digital Twin applications in historical masonry buildings: The integration between numerical and experimental reality. Comput Struct 2020;238:106282. https://doi.org/10.1016/j.compstruc.2020.106282.

[21] Tajali M, Ataei S, Miri A, Ahmadi E, Kashani MM. Seismic assessment of a railway masonry arch bridge using sensor-based model updating. Proceedings of the Institution of Civil Engineers - Bridge Engineering.0:1-12, 10.1680/jbren.22.00019.

[22] Bayraktar A, Altunişik AC, Birinci F, Sevim B, Türker T. Finite-element analysis and vibration testing of a two-span masonry arch bridge. J Perform Constr Facil 2010;24:46–52.

[23] Aytulun E, Soyoz S, Karcioglu E. System Identification and Seismic Performance Assessment of a Stone Arch Bridge. J Earthq Eng 2022;26:723–43. https://doi.org/10.1080/13632469.2019.1692740.

[24] Bautista-De Castro Á, Sánchez-Aparicio LJ, Carrasco-García P, Ramos LF, González-Aguilera D. A multidisciplinary approach to calibrating advanced numerical simulations of masonry arch bridges. Mech Syst Sig Process 2019;129:337–65. https://doi.org/10.1016/j.ymssp.2019.04.043.

[25] Altunişik AC, Okur FY, Genç AF, Günaydin M, Karahasan O. Automated Model Updating Effect on the Linear and Nonlinear Dynamic Responses of Historical Masonry Structures. Exp Tech 2018;42:605–21. https://doi.org/10.1007/s40799-018-0271-0.

[26] Yavartanoo F, Kang THK. Retrofitting of unreinforced masonry structures and considerations for heritage-sensitive constructions. Journal of Building Engineering 2022;49:103993. https://doi.org/10.1016/j.jobe.2022.103993.

[27] Valluzzi MR, Modena C, de Felice G. Current practice and open issues in strengthening historical buildings with composites. Mater Struct 2014;47:1971–85. https://doi.org/10.1617/s11527-014-0359-7.

[28] D'Ambrisi A, Focacci F, Luciano R, Alecci V, De Stefano M. Carbon-FRCM materials for structural upgrade of masonry arch road bridges. Compos B Eng 2015;75:355–66.

[29] Zampieri P, Simoncello N, Gonzalez-Libreros J, Pellegrino C. Evaluation of the vertical load capacity of masonry arch bridges strengthened with FRCM or SFRM by limit analysis. Eng Struct 2020;225:111135.

[30] Simoncello N, Zampieri P, Gonzalez-Libreros J, Perboni S, Pellegrino C. Numerical analysis of an FRP-strengthened masonry arch bridge. Frontiers in Built Environment 2020;6:7.

[31] Tao Y, Stratford T, Chen J-F. Behaviour of a masonry arch bridge repaired using fibre-reinforced polymer composites. Eng Struct 2011;33:1594–606.

[32] Bayraktar A, Hökelekli E. Seismic performances of different spandrel wall strengthening techniques in masonry arch bridges. International Journal of Architectural Heritage 2021;15:1722–40.

[33] Behnamfar F, Afshari M. Collapse Analysis and Strengthening of Stone Arch Bridges Against Earthquake. International Journal of Architectural Heritage 2013;7:1–25. https://doi.org/10.1080/15583058.2011.606594.

[34] Shabani A, Feyzabadi M, Kioumarsi M. Model updating of a masonry tower based on operational modal analysis: The role of soil-structure interaction. Case Stud Constr Mater 2022;16:e00957.

[35] Reynders E. System identification methods for (operational) modal analysis: review and comparison. Arch Comput Meth Eng 2012;19:51–124.

[36] Tan Y, Zhang L. Computational methodologies for optimal sensor placement in structural health monitoring: A review. Struct Health Monit 2020;19:1287–308.

[37] Arora V. Comparative study of finite element model updating methods. J Vib Control 2011;17:2023–39.

[38] Mottershead JE, Link M, Friswell MI. The sensitivity method in finite element model updating: A tutorial. Mech Syst Sig Process 2011;25:2275–96.

[39] Shabani A, Kioumarsi M, Zucconi M. State of the art of simplified analytical methods for seismic vulnerability assessment of unreinforced masonry buildings. Eng Struct 2021;239:112280. https://doi.org/10.1016/j.engstruct.2021.112280.

[40] Jalayer F, Cornell C. Alternative non-linear demand estimation methods for probability-based seismic assessments. Earthq Eng Struct Dyn 2009;38:951–72.

[41] Baker JW. Efficient Analytical Fragility Function Fitting Using Dynamic Structural Analysis. Earthq Spectra 2015;31:579–99. https://doi.org/10.1193/021113eqs025m.

[42] Bougia P. Ancient bridges in Greece and Coastal Asia Minor. USA: University of Pennsylvania; 1996.

[43] Pagani M, Garcia-Pelaez J, Gee R, Johnson K, Poggi V, Silva V, et al. The 2018 version of the Global Earthquake Model: hazard component. Earthq Spectra 2020;36:226–51.

[44] Stiros S, Papageorgiou S, Kontogianni V, Psimoulis P. Church repair swarms and earthquakes in Rhodes Island. Greece Journal of Seismology 2006;10:527–37. https://doi.org/10.1007/s10950-006-9035-x.

[45] Shabani A, Skamantzari M, Tapinaki S, Georgopoulos A, Plevris V, Kioumarsi M. 3D simulation models for developing digital twins of heritage structures: challenges and strategies. Procedia Struct Integrity 2022;37:314–20. https://doi.org/10.1016/j.prostr.2022.01.090.

[46] Tapinaki S, Skamantzari M, Anastasiou A, Koutros S, Syrokou E, Georgopoulos A. 3D Holistic documentation of heritage monuments in Rhodes. The International Archives of Photogrammetry, Remote Sensing and Spatial Information Sciences 2021;46:739–44.

[47] DIANA. DIANA FEA, Diana User's Manual, Release 10.4. In DIANA FEA BV, Delft University of Technology, Netherland. 2020.

[48] Anderson JG, Lee Y, Zeng Y, Day S. Control of strong motion by the upper 30 meters. Bull Seismol Soc Am 1996;86:1749–59.

[49] Tabatabaiefar HR, Massumi A. A simplified method to determine seismic responses of reinforced concrete moment resisting building frames under influence of soil–structure interaction. Soil Dyn Earthq Eng 2010;30:1259–67. https://doi.org/10.1016/j.soildyn.2010.05.008.

[50] Güllü H, Karabekmez M. Effect of near-fault and far-fault earthquakes on a historical masonry mosque through 3D dynamic soil-structure interaction. Eng Struct 2017;152:465–92. https://doi.org/10.1016/j.engstruct.2017.09.031.

[51] Torabi H, Rayhani MT. Three dimensional Finite Element modeling of seismic soil–structure interaction in soft soil. Comput Geotech 2014;60:9–19. https://doi.org/10.1016/j.compgeo.2014.03.014.

[52] Kioumarsi M, Plevris V, Shabani A. Vulnerability assessment of cultural heritage structures. In ECCOMAS Congress 2022 - 8th European Congress on Computational Methods in Applied Sciences and Engineering. Oslo, Norway. 2022.

[53] Fanning PJ, Boothby TE. Three-dimensional modelling and full-scale testing of stone arch bridges. Comput Struct 2001;79:2645–62. https://doi.org/10.1016/S0045-7949(01)00109-2.

[54] Homaei F, Yazdani M. The probabilistic seismic assessment of aged concrete arch bridges: The role of soil-structure interaction. Structures 2020;28:894–904. https://doi.org/10.1016/j.istruc.2020.09.038.

[55] Psycharis IN, Avgenakis E, Taflampas IM, Kroustallaki M, Farmakidou E, Pikoula M, et al. Seismic Response of the Temple of Pythian Apollo in Rhodes Island and Recommendations for Its Restoration. In: In. Cham: Springer International Publishing; 2019. p. 160–77.

[56] Ghiassi B, Vermelfoort AT, Lourenço PB. Chapter 7 - Masonry mechanical properties. In: Ghiassi B, Milani G, editors. Numerical Modeling of Masonry and Historical Structures. Woodhead Publishing; 2019. p. 239–61.
[57] CEB-FIP. CEB-FIP Model Code 90, CEB Bulletin D'Information No. 213/214. In. London (UK): May. 1993.
[58] Shabani A, Kioumarsi M, Plevris V. Performance-based Seismic Assessment of a Historical Masonry Bridge: Effect of Pulse-like Excitations. Frontiers of Structural and Civil. Engineering 2023. https://doi.org/10.1007/s11709-023-0972-z.
[59] Kuhlemeyer RL, Lysmer J. Finite element method accuracy for wave propagation problems. Journal of the Soil Mechanics and Foundations Division 1973;99:421–7.
[60] Shabani A, Kioumarsi M. Optimal sensor placement techniques for modal identification of historical masonry structures. Procedia Struct Integrity 2022;42: 147–54. https://doi.org/10.1016/j.prostr.2022.12.018.
[61] SVIBS. ARTeMIS Modal, Structural Vibration Solution. In. Aalborg, Denmark 2022.
[62] Zahid FB, Ong ZC, Khoo SY. A review of operational modal analysis techniques for in-service modal identification. J Braz Soc Mech Sci Eng 2020;42:398. https://doi.org/10.1007/s40430-020-02470-8.
[63] FEMtools. Dynamic Design Solutions, FEMtools 4 user guide. In. Leuven, Belgium. 2021.
[64] Hokelekli E, Yilmaz BN. Effect of Cohesive Contact of Backfill with Arch and Spandrel Walls of a Historical Masonry Arch Bridge on Seismic.
[65] Hardin BO, Drnevich VP. Shear Modulus and Damping in Soils: Design Equations and Curves. Journal of the Soil Mechanics and Foundations Division 1972;98: 667–92. https://doi.org/10.1061/JSFEAQ.0001760.
[66] Nielsen AH. Absorbing boundary conditions for seismic analysis in ABAQUS. In ABAQUS users' conference. 2006. p. 359-76.
[67] Longo M, Sousamli M, Korswagen PA, van Staalduinen P, Rots JG. Sub-structure-based 'three-tiered' finite element approach to soil-masonry-wall interaction for light seismic motion. Eng Struct 2021;245:112847. https://doi.org/10.1016/j.engstruct.2021.112847.
[68] Gönen S, Soyöz S. Reliability-based seismic performance of masonry arch bridges. Struct Infrastruct Eng 2021:1–16. https://doi.org/10.1080/15732479.2021.1918726.
[69] Woessner J, Laurentiu D, Giardini D, Crowley H, Cotton F, Grünthal G, et al. The 2013 European seismic hazard model: key components and results. Bull Earthq Eng 2015;13:3553–96.
[70] Boore DM, Atkinson GM. Ground-motion prediction equations for the average horizontal component of PGA, PGV, and 5%-damped PSA at spectral periods between 0.01 s and 10.0 s. Earthq Spectra 2008;24:99–138.
[71] Pagani M, Monelli D, Weatherill G, Danciu L, Crowley H, Silva V, et al. OpenQuake engine: An open hazard (and risk) software for the global earthquake model. Seismol Res Lett 2014;85:692–702.
[72] Kohrangi M, Bazzurro P, Vamvatsikos D, Spillatura A. Conditional spectrum-based ground motion record selection using average spectral acceleration. Earthq Eng Struct Dyn 2017;46:1667–85.
[73] Chiou B, Darragh R, Gregor N, Silva W. NGA project strong-motion database. Earthq Spectra 2008;24:23–44.
[74] Lin T, Harmsen SC, Baker JW, Luco N. Conditional spectrum computation incorporating multiple causal earthquakes and ground-motion prediction models. Bull Seismol Soc Am 2013;103:1103–16.
[75] Bertolesi E, Milani G, Lopane FD, Acito M. Augustus Bridge in Narni (Italy): Seismic Vulnerability Assessment of the Still Standing Part, Possible Causes of Collapse, and Importance of the Roman Concrete Infill in the Seismic-Resistant Behavior. International Journal of Architectural Heritage 2017;11:717–46. https://doi.org/10.1080/15583058.2017.1300712.
[76] Estevan L, Baeza FJ, Bru D, Ivorra S. Stone masonry confinement with FRP and FRCM composites. Constr Build Mater 2020;237:117612. https://doi.org/10.1016/j.conbuildmat.2019.117612.
[77] Babaeidarabad S, Caso FD, Nanni A. URM Walls Strengthened with Fabric-Reinforced Cementitious Matrix Composite Subjected to Diagonal Compression. J Compos Constr 2014;18:04013045. https://doi.org/10.1061/(ASCE)CC.1943-5614.0000441.
[78] Wang X, Ghiassi B, Oliveira DV, Lam CC. Modelling the nonlinear behaviour of masonry walls strengthened with textile reinforced mortars. Eng Struct 2017;134: 11–24. https://doi.org/10.1016/j.engstruct.2016.12.029.
[79] Arboleda D, Carozzi FG, Nanni A, Poggi C. Testing Procedures for the Uniaxial Tensile Characterization of Fabric-Reinforced Cementitious Matrix Composites. J Compos Constr 2016;20:04015063. https://doi.org/10.1061/(ASCE)CC.1943-5614.0000626.
[80] Bertolesi E, Carozzi FG, Milani G, Poggi C. Numerical modeling of Fabric Reinforce Cementitious Matrix composites (FRCM) in tension. Constr Build Mater 2014;70: 531–48.
[81] Scacco J, Ghiassi B, Milani G, Lourenço PB. A fast modeling approach for numerical analysis of unreinforced and FRCM reinforced masonry walls under out-of-plane loading. Compos B Eng 2020;180:107553.
[82] Tedesco A, Forestieri G. FRCM reinforcement systems in historical masonries of savuto castle, italy. J Archit Eng 2019;25:05019003.